Modeling and nonlinear analysis of a coupled thermo-mechanical dual-rotor system*

Zeyuan Chang[1,+], Lei Hou[1,†], Pierangelo Masarati[2], Rongzhou Lin[1], Zhonggang Li[1], Yushu Chen [1]

[1]School of Astronautics, Harbin Institute of Technology, Harbin 150001, People's Republic of China

[2]Department of Aerospace Science and Technology, Politecnico di Milano, Milano 20156, Italy

[†]Corresponding author

[+]Currently visiting PhD Student at[1]

July 31, 2024

Abstract

Analyzing the nonlinear characteristics of dual-rotor systems under thermo-mechanical (TM) coupling situations is critical, as operational conditions should be accurately determined, to avoid potential thermally-induced failures. This paper proposes the coupled TM model of a dual-rotor system, which considers multiple nonlinearities and heat generation of four bearings that couple the mechanical and thermal fields. Heat dissipation controlled by lubricant flow rates is introduced into the model to simulate different TM coupling degrees. Nonlinear phenomena and stability evolution are analyzed by the modified incremental harmonic balance method (IHB) at primary resonance regions. An increase in TM coupling degrees can lead to more bifurcation points, resonance regions with lower frequencies, larger vibration responses, and unstable regions. It can also transform resonance hysteresis phenomena into more complex nonlinear phenomena and some saddle-node bifurcation points into Neimark-Sacker bifurcation points. The reason for these transformations is that the effective radial clearance (RC) of bearings changes with rotation speed and thermal expansion. Temperature nonlinearities are induced by the radial bearing loads and the lubricant viscosity, which are investigated by various generalized nonlinear thermal forces. These findings can help further understand nonlinear coupled TM problems of complex dual-rotor systems.

1 Introduction

With the development of the aviation industry, dual-rotor systems have gradually become the basic configuration for the rotating part of aero-engines [1]. Nonlinearities in the system are mainly induced by the bearings, which feature time-varying nonlinear stiffness, lubricant friction, and cage instability. Nonlinear dynamic characteristic responses of dual-rotor systems, including resonance hysteresis phenomena, hardening/softening characteristics [2], multiple solutions [3], and vibration response evolution [4] have been analyzed in detail at the primary resonance regions [5] or other combination resonance regions [6, 7]. Besides, rotor systems often operate under the influence of multiphysical excitation sources. The mechanical field coexists with thermal, fluid, electro/magnetic fields, and possibly more. Many couplings may occur, such as torsional-lateral vibration [8], thermo-mechanical (TM) [9], fluid-structure [10, 11], and electro-mechanical [12] coupling phenomena. Higher operating temperatures are commonplace in many rotor systems. Although rolling bearings can sustain operating temperatures, their nonlinear stiffness is easily affected by temperature variation, leading to intricate nonlinear characteristic variations and vibration problems [13, 14]. Thermally-induced failures may occur in case of preload change in rolling bearings, insufficient lubricant supply, and harsh environmental conditions [15]. TM coupling stands as an important concern in the analysis of optimal operational conditions for dual-rotor systems, owing to the challenges in discerning the variation patterns of coupling characteristics.

There is a strong need for better modeling of rolling bearings, whose heat generation is affected by dynamic characteristics and nonlinear stiffness is affected by thermal characteristics, to establish a coupled TM model of a dual-rotor system. During the last two decades, continuous models refinements appeared in the heat generation and transfer literature. One of the first thermal models is proposed by Bossmanns and Tu [16]. The analysis in [17] subsequently examines the impact of bearing assembly tolerance on the spindle bearing compliance, which considers both the Hertzian contact model and the component deformation of the bearing components with temperature variation. Since then, various complex coupled TM models have been established for deep-groove ball bearings [18], cylindrical roller bearings [19], active magnetic bearings [20], foil-air journal bearings [21], angular contact ball bearings [22], floating ring bearings [23] and offset-halves journal bearings [24]. Bearing models with more than two coupled physical fields are presented to analyze skidding behavior, over-skidding behavior, and other transient nonlinear dynamic behaviors, e.g., the coupled kinematic-Hertzian contact-thermo-elasto-hydrodynamic model in [25], the coupled thermo-elasto-hydrodynamic model in [26] and the coupled fluid-solid-heat model in [27]. Although most of the coupled models mainly focus on the bearing and assembly components, their development lays the foundation for investigating the rotor system's nonlinear TM characteristics.

The analysis of coupled TM problems of rotors starts from one of the pioneering works of Goldman and Muszynska [28], which investigates the thermal effects of rotor-to-stator rub on the rotor system's vibration response. The TM

problem is partially coupling-free, considering the slow variation of the thermal process. A transient TM analysis is carried out in [29] to estimate the turbine blade tip clearance of a small gas turbine engine. Liu et al. [30] investigated the nonlinear dynamic characteristics of a computerized numerical control lathe spindle-bearing system considering thermal effects. The vibration response of a gear-rotor-bearing system is analyzed with steady-state temperature in [31]. Bifurcation characteristics of a rotor-bearing system are investigated in [32] with temperature-dependent lubricant viscosity under different temperatures. A functionally graded shaft-disk rotor system's dynamic characteristics in the thermal field are analyzed in [33], which presents the effects of thermo-physical properties of the material on the vibration responses. All the results show that the system stiffness and the lubricant viscosity affected by the temperature can lead to more violent and complex variations in dynamic characteristics. The nonlinear temperature variations of a dual-rotor system are analyzed in [34], subjected to the dynamic load of the bearings, which shows the corresponding nonlinear phenomena in temperature variations. Transient heat transfer and core temperatures in closed compressor rotors are studied in [35, 36] and validated by experiments. The above-mentioned literature mainly focuses on the one-way coupling, assuming that the vibration responses and the temperature affect each other unilaterally.

Due to the requirements for more precise predictions of simultaneous changes in dynamic and thermal characteristics, some fully coupled TM problems of rotor systems have been investigated since the late 2010s. A dual-rotor gas turbine engine's long duration blade loss are simulated in [37], which uses a nonlinear ball bearing model with the Hertzian contact model and a thermal model with the thermal expansion of bearing components during the blade loss event. The effects of surface waviness on heat generation and component deformation of the touchdown bearing is investigated in [38], based on the rotor supported by a deep groove ball bearing and a pair of angular contact ball bearings. Effects of angular ball bearings' thermal deformations on the optical grinding motorized spindle's vibration response are presented in [39] to analyze the spindle-tool assembly dynamics. Hu et al. [40] used the nonlinear tribo-dynamic model to analyze a spur gear drive's temperature rise and tooth wear caused by time-varying friction under loss-of-lubrication conditions. Based on the thermo-hydrodynamic lubrication bearing model, Peixoto et al. [41] analyzed the nonlinear dynamic characteristics of a turbocharger-bearing system. The interaction relationship among the force, lubrication, and temperature for the rotor-bearing system of a high-speed train is investigated in [42]. Gao et al. [43] analyzed the nonlinear coupled TM characteristics of a simplified dual-rotor system with an inter-shaft bearing by numerical iteration. The analysis of the heat generation and vibration response of the ball screw feed system is reported in [44]. It shows that the coupling induces multiple jump phenomena and more bifurcation points in the system. A closed-loop iterative modeling method is proposed in [45] to investigate TM characteristics of high-speed motorized spindle systems. Hassini [46] studied the influence of a hot spot on the dynamic characteristics of a flexible rotor supported by oil journal bearings and conducted spiral vibrations'

stability discrimination in simulations and experiments. In [9, 47], Chang et al. analyzed the nonlinear dynamic and thermal coupling characteristics of a rotor-ball bearing system using a step-by-step iterative method and proposed a modified incremental harmonic balance (IHB) method for solving coupled TM problems of rotor-bearing systems in the frequency domain.

Most previous works are limited to the one-way coupling or low-dimensional models without more than one nonlinear bearing in the rotor system, making it difficult to investigate the TM coupling phenomena induced by the combined effects of multiple bearings' elastic restoring forces and heat generation in practical engineering applications. Moreover, analyzing the continuous evolution patterns of nonlinear TM characteristics can be very challenging, since different TM coupling degrees have not been simulated in literature, and the complex coupled TM rotor model's calculation time is unacceptably long caused by the essentially different velocities of vibration responses and temperature variations [48]. Besides, the unstable solutions are difficult to obtain, owing to multiple nonlinearities and a high degree-of-freedom (DoF).

The motivation of this paper is to present a novel coupled TM model of a dual rotor system with multiple nonlinear bearings. Herein, the two rotors are supported by four nonlinear bearings, accounting for the influence of thermal expansion on the bearings' contact states. Meanwhile, the frictional heat generated by the bearings is transferred to the rotors, thus coupling the thermal field with the mechanical field of the system. Based on the model, different TM coupling degrees are simulated through heat dissipation controlled by lubricant flow rates. The modified IHB method is employed to solve the governing equations of the coupled TM model, obtaining all periodic solutions, including unstable ones, which enable us to analyze the nonlinear phenomena and stability evolution in dynamic and thermal characteristics. New phenomena are found, such as the transformations from resonance hysteresis phenomena to more complex nonlinear phenomena and from saddle-node bifurcation points to Neimark-Sacker bifurcation points. The results provide the theoretical foundation for designing the operational conditions of rotor systems to suppress harmful vibrations and temperatures.

The paper is organized as follows. In Section 2, the dynamic model of the dual-rotor system as a discretized one-dimensional continuum is developed using the finite element (FE) method. In Section 3, the thermal model is developed using the lumped-parameter thermal network (LPTN) method. In Section 4, the periodic solutions of the governing equations are computed using the modified IHB method. In Section 5, the coupled TM dual-rotor system's nonlinear characteristics are analyzed and discussed. Finally, Section 6 draws the conclusions and final remarks.

2 Dynamic model of the dual-rotor system

The object of this work is a dual-rotor system with a low-pressure (LP) rotor and a high-pressure (HP) rotor. The rotors' compressor disks and turbine disks

are named as LPC, LPT, HPC and HPT disk, correspondingly. The system is discretized into 18 dynamic nodes using the FE method (see Fig. 1), as a discretized one-dimensional continuum. The LP rotor is supported by the 1# ball bearing (at dynamic node 1), a linear elastic support (at dynamic node 4), the 3# roller bearing (an inter-shaft bearing between dynamic node 8 and dynamic node 14) and the 4# roller bearing (at dynamic node 11). The HP rotor is supported by the 2# ball bearing (at dynamic node 12) and the 3# inter-shaft roller bearing. ω_1 is the rotation speed of the LP rotor. $\omega_2 = \lambda\omega_1$ is the rotation speed of the HP rotor, where λ is the speed ratio of the HP rotor and LP rotor. Note that all bearing models are nonlinear with Hertzian contact stiffness $k_{\mathrm{b}1}$, $k_{\mathrm{b}2}$, $k_{\mathrm{r}3}$ and $k_{\mathrm{r}4}$ corresponding to the bearing number. Dynamic node 1's geometric center is chosen as the coordinate origin O and coordinate axis Oz aligns with the shaft centerline direction. The motion of each node can be described with four DoFs: the vertical displacement x, the horizontal displacement y, the rotational angle θ_x around the x axis, and the rotational angle θ_y around the y axis. Consequently, the dynamic model has 72 DoFs. During the modeling process, there are assumptions as follows:

- LPC disk, LPT disk, HPC disk, and HPT disk are rigid disks with gyroscopic effects.
- The shaft element between two adjacent nodes is an annular hollow beam with equal cross-section, and modeled using the Timoshenko beam model without considering the torsional and axial vibration.
- The inner ring of the bearings and the rotation shaft have an interference fit. Except for the inter-shaft bearing, the outer rings of bearings are mounted to the rigid bearing housings. Rolling elements of the bearings do pure rolling between the inner and outer rings without considering the interaction force between the rolling element and the cage, the centrifugal force and the gyroscopic effect of the rolling element.
- For different rotation speeds, the effective radial clearance (RC) of each bearing vary dynamically under bearing components' thermal expansion without considering dimensional variation in other structures. The thermal expansion of bearings and their assembly parts are linear functions of temperature.

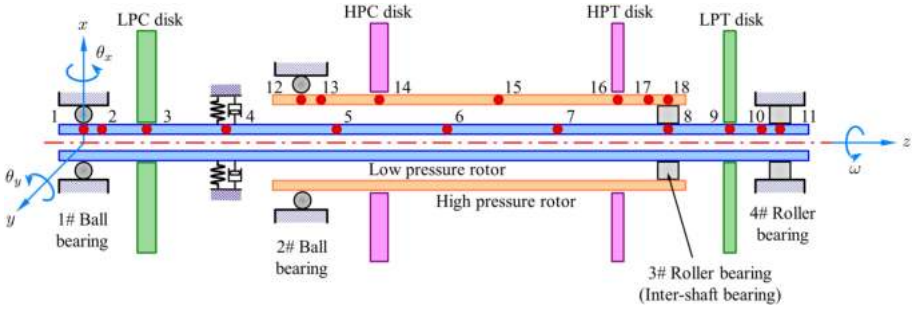

Figure 1: Schematic diagram of the dual-rotor system.

2.1 Nonlinear bearing models under thermal expansion

Bearings are usually simplified as linear supports or only the inter-shaft bearing is established as a nonlinear model in the traditional dual-rotor system modeling process. Although the linear bearing model can analyze dynamic characteristics, it inevitably ignores the coupling effect between multiple bearing nonlinearities. Besides, the friction torque of bearings is one of the main sources of heat generation. Nonlinear bearing models can better reflect the heat generation and transfer, to further detect nonlinear characteristics under TM coupling.

Structure parameters of the bearing and assembly parts for the 1# ball bearing and the 3# inter-shaft roller bearing are illustrated in Fig. 2 as the representations of all bearings. Detailed system parameters are provided in Appendix A.

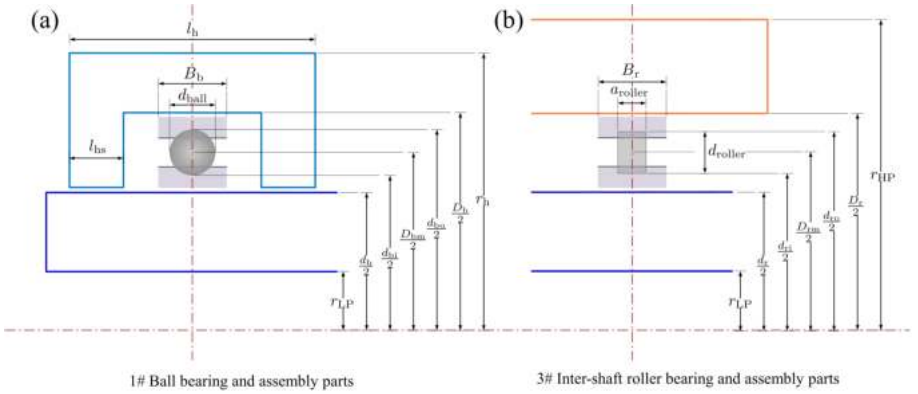

Figure 2: Structure parameters of the bearing and assembly parts (a) for the 1# ball bearing. (b) for the 3# inter-shaft roller bearing.

Taking the 1# ball bearing as an example, the deformations of rolling elements and the inner ring under thermal expansion can be obtained as

$$u_{\mathrm{b}} = \Gamma_{\mathrm{b}} d_{\mathrm{ball}} (T_{\mathrm{b}} - T_{\infty}), \tag{1a}$$

$$u_{\mathrm{i}} = \Gamma_{\mathrm{i}} d_{\mathrm{bi}} (T_{\mathrm{i}} - T_{\infty}), \tag{1b}$$

where T_{b}, T_{i} and T_{∞} are the temperature of rolling elements, the inner ring and ambient, respectively.

Since the outer rings of bearings are interfered by bearing housings or the rotation shaft, it cannot expand without limitation. Its radial expansion can be calculated as [49]

$$u_{\mathrm{o}} = \frac{\Gamma_{\mathrm{o}}}{3} \frac{(1+\mu) d_{\mathrm{bo}}}{d_{\mathrm{bo}} + d_{\mathrm{h}}} \left[(T_{\mathrm{o}} - T_{\infty})(2d_{\mathrm{bo}} + d_{\mathrm{h}}) + (T_{\mathrm{h}} - T_{\infty})(2d_{\mathrm{h}} + d_{\mathrm{bo}}) \right], \tag{2}$$

where $d_{\mathrm{h}} = 2r_{\mathrm{h}}$, T_{o} and T_{h} are the temperatures of the outer ring and the bearing housing, respectively. For the 3# inter-shaft roller bearing, $u_{\mathrm{o}} =$

$\frac{\Gamma_o}{3}\frac{(1+\mu)d_{ro}}{d_{ro}+d_{HP}}[(T_o - T_\infty)(2d_{ro} + d_{HP}) + (T_{HP} - T_\infty)(2d_{HP} + d_{ro})]$, where $d_{HP} = 2r_{HP}$ and T_{HP} is the temperature of the corresponding high-pressure rotation shaft element.

The elastic deformation between the kth rolling element ($k = 1, 2, \cdots, N_{ball}$) and rings under thermal expansion can be expressed as

$$\delta_k = (x_{2i-1} - x_{2o-1})\cos\theta_k + (y_{2i-1} - y_{2o-1})\sin\theta_k - \delta_e, \tag{3}$$

where i and o denote the node number corresponding to the locations of the bearing's inner ring and outer ring, respectively. For example, $i = 1$ and $x_{2o-1} = y_{2o-1} = 0$ are for the 1# ball bearing because the bearing housing is mounted on the ground without deformation. $i = 8$ and $o = 18$ are for the 3# inter-shaft roller bearing.

The effective RC of the bearing can be defined as $\delta_e = \delta_0 + \delta_v$. δ_0 is the initial RC. $\delta_v = -(u_b + \frac{u_i - u_o}{2})$ is the RC variation under thermal expansion. $\theta_k = \frac{2\pi}{N_{ball}}(k-1) + \omega_c t$ is the angular position of the kth rolling element at any time t. N_{ball} is the number of rolling elements. The bearing cage's rotation speed is expressed as $\omega_c = \frac{d_{bi}\omega_i + d_{bo}\omega_o}{d_{bi}+d_{bo}}$.

The bearings' elastic restoring forces can be calculated as

$$\begin{bmatrix} F_x \\ F_y \end{bmatrix} = k_{b1}\sum_{k=1}^{N_{ball}} (\delta_k)^n H(\delta_k) \begin{bmatrix} \cos\theta_k \\ \sin\theta_k \end{bmatrix}, \tag{4}$$

where Heaviside function $H(\cdot) = \begin{bmatrix} 1 \\ 0 \end{bmatrix} \begin{matrix} (\cdot > 0) \\ (\cdot \le 0) \end{matrix}$. The value of coefficient n is dictated by the bearing contact type, $n = 3/2$ for ball bearings and $n = 10/9$ for roller bearings.

The radial bearing loads can be given as

$$F_b = k_{b1}\sum_{k=1}^{N_{ball}} (\delta_k)^n H(\delta_k) \tag{5}$$

for calculating the friction torque to estimate the frictional heat of the system.

2.2 Motion equations

The motion equations of rigid disks are expressed as

$$\begin{aligned} \mathbf{M}_d\ddot{\mathbf{q}}_{d1} + \Omega\mathbf{J}_d\dot{\mathbf{q}}_{d2} &= \mathbf{F}_{d1} + \mathbf{F}_{gd1}, \\ \mathbf{M}_d\ddot{\mathbf{q}}_{d2} - \Omega\mathbf{J}_d\dot{\mathbf{q}}_{d1} &= \mathbf{F}_{d2} + \mathbf{F}_{gd2}, \end{aligned} \tag{6}$$

where $\mathbf{q}_{d1} = \begin{bmatrix} x & \theta_x \end{bmatrix}^T$, $\mathbf{q}_{d2} = \begin{bmatrix} y & \theta_y \end{bmatrix}^T$, $\mathbf{M}_d = \begin{bmatrix} m & 0 \\ 0 & J_d \end{bmatrix}$ and $\mathbf{J}_d = \begin{bmatrix} 0 & 0 \\ 0 & J_p \end{bmatrix}$. Ω is the rotation speed of the corresponding node. The excitation force matrices $\mathbf{F}_{d1}$ and $\mathbf{F}_{d2}$ are induced by the eccentricities of disks, where the

forces are written as $F_{\mathrm{en}x} = m\omega^2 e\cos\omega t$ and $F_{\mathrm{en}y} = m\omega^2 e\sin\omega t$, respectively. m, e and ω are the mass, eccentricity and rotation speed of disks, respectively. The excitation force matrices $\mathbf{F}_{\mathrm{gd1}}$ and $\mathbf{F}_{\mathrm{gd2}}$ are induced by the gravity of disks.

The motion equations of rotation shafts are expressed as

$$\begin{aligned}\mathbf{M}_{\mathrm{s}}\ddot{\mathbf{q}}_{\mathrm{s1}} + \Omega\mathbf{J}_{\mathrm{s}}\dot{\mathbf{q}}_{\mathrm{s2}} + \mathbf{K}_{\mathrm{s}}\mathbf{q}_{\mathrm{s1}} &= \mathbf{F}_{\mathrm{s1}} + \mathbf{F}_{\mathrm{gs1}},\\ \mathbf{M}_{\mathrm{s}}\ddot{\mathbf{q}}_{\mathrm{s2}} - \Omega\mathbf{J}_{\mathrm{s}}\dot{\mathbf{q}}_{\mathrm{s1}} + \mathbf{K}_{\mathrm{s}}\mathbf{q}_{\mathrm{s2}} &= \mathbf{F}_{\mathrm{s2}} + \mathbf{F}_{\mathrm{gs2}},\end{aligned} \tag{7}$$

where $\mathbf{q}_{\mathrm{s1}} = \begin{bmatrix} x_1 & \theta_{x1} & x_2 & \theta_{x2}\end{bmatrix}^{\mathrm{T}}$, $\mathbf{q}_{\mathrm{s2}} = \begin{bmatrix} y_1 & \theta_{y1} & y_2 & \theta_{y2}\end{bmatrix}^{\mathrm{T}}$, the matrices $\mathbf{M}_{\mathrm{s}}$, $\mathbf{J}_{\mathrm{s}}$ and $\mathbf{K}_{\mathrm{s}}$ are given in Appendix B. Ω is the rotation speed of the corresponding node. The excitation force matrices $\mathbf{F}_{\mathrm{s1}}$ and $\mathbf{F}_{\mathrm{s2}}$ consist of the elastic restoring forces of bearings given in Section 2.1. The excitation force matrices $\mathbf{F}_{\mathrm{gs1}}$ and $\mathbf{F}_{\mathrm{gs2}}$ are induced by the gravity of rotation shafts.

By combining Eq. (6) and Eq. (7), the motion equations of the system are expressed as

$$\mathbf{M}_{\mathrm{M}}\ddot{\mathbf{X}}_{\mathrm{M}} + (\mathbf{C}_{\mathrm{M}} + \Omega\mathbf{J}_{\mathrm{M}})\dot{\mathbf{X}}_{\mathrm{M}} + \mathbf{K}_{\mathrm{M}}\mathbf{X}_{\mathrm{M}} + \hat{\mathbf{F}}_{\mathrm{M}}(\mathbf{X}) = \mathbf{F}_{\mathrm{M}}(t), \tag{8}$$

where $q(t) = [x_1 \quad \theta_{x1} \quad \dots \quad x_n \quad \theta_{xn} \quad y_1 \quad \theta_{y1} \quad \dots \quad y_n \quad \theta_{yn}]^{\mathrm{T}}$ denotes the generalized coordinate vector, $n = \mathrm{nDoF}_{\mathrm{Dynamic}}$ represents the number of dynamic DoFs. $(\ \dot{}\ )$ and $(\ \ddot{}\ )$ denote derivatives with respect to time t. Ω is the rotation speed of the corresponding node. The damping matrix $\mathbf{C}_{\mathrm{M}}$ is a proportional damping matrix and given by $\mathbf{C}_{\mathrm{M}} = a_0\mathbf{M}_{\mathrm{M}} + a_1\mathbf{K}_{\mathrm{M}}$. The nonlinear force matrix $\hat{\mathbf{F}}_{\mathrm{M}}(\mathbf{X})$ consists of the elastic restoring forces of bearings on the corresponding node. The harmonic matrix $\mathbf{F}_{\mathrm{M}}(t)$ consists of eccentricity excitation forces and gravity of rotors on the corresponding node.

3 Thermal model of the dual-rotor system

The thermal model of the dual-rotor system is developed using the LPTN method. The thermal field of the system is discretized into 66 isothermal elements represented by thermal nodes (see Fig. 3). Hence, the thermal model is described with 66 DoFs. The heat transfer networks of the bearing and assembly parts for the 1# ball bearing and the 3# inter-shaft roller bearing are illustrated in Fig. 4 as the representations of all thermal resistance connection cases among the isothermal elements. Thermal resistances of ambient $\mathbf{R}_{\mathrm{amb}}$, shaft $\mathbf{R}_{\mathrm{shaft}}$ and bearing housing $\mathbf{R}_{\mathrm{housing}}$ are constant thermal resistances, because they are not time-varying at a fixed rotation speed. On the other hand, bearing thermal resistances $\mathbf{R}_{\mathrm{bear}}$ change with the radial bearing loads. Lubricant thermal resistances $\mathbf{R}_{\mathrm{lub}}$ change with the lubricant viscosity. During the thermal modeling process, there are assumptions as follows:

- The rolling elements, the inner ring and the outer ring of a bearing, are modeled as three lumped-mass isothermal elements because their Biot number is small enough (Bi ¡ 0.1).
- The bearing cages do not have separate thermal nodes, and their masses are added to the rolling elements.

- The heat of the system comes from the frictional heat generated by multiple bearings without considering the heat transferred to the system from the combustion chamber or other structures.
- The heat transfer process consists of heat conduction and heat convection without considering heat radiation at a lower temperature.

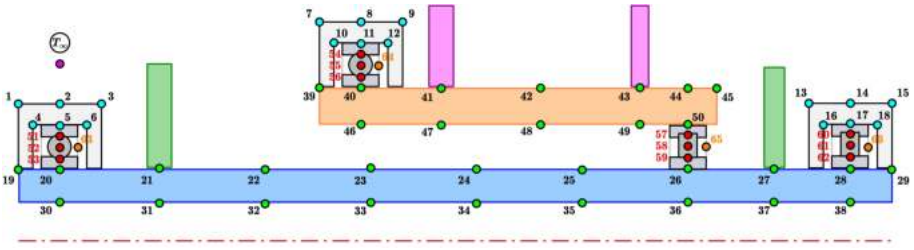

Figure 3: Thermal node distribution of the dual-rotor system.

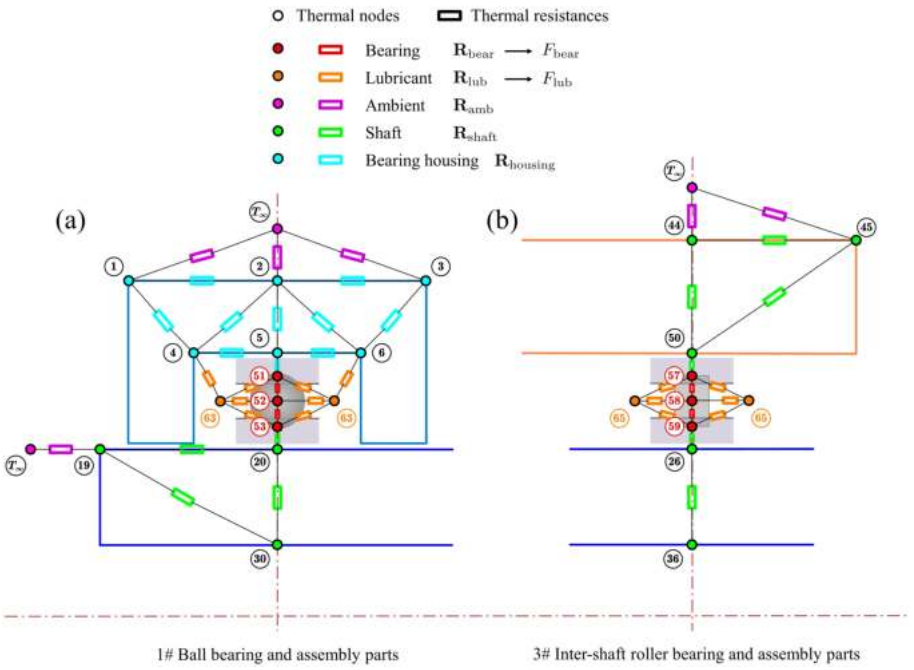

Figure 4: Heat transfer networks of the bearing and assembly parts (a) for the 1# ball bearing. (b) for the 3# inter-shaft roller bearing.

3.1 Heat generation of bearings

The total friction torque of bearings is given by [50]

$$M = M_{\mathrm{l}} + M_{\mathrm{v}}, \tag{9}$$

where friction torques M_{l} and M_{v} are estimated as

$$M_{\mathrm{l}} = f_{\mathrm{l}} F_{\mathrm{b}} D_{\mathrm{m}}, \tag{10}$$

$$M_{\mathrm{v}} = \begin{cases} 10^{-7} f_{\mathrm{v}} (\nu n)^{2/3} {D_{\mathrm{m}}}^3 & \nu n \geq 2000 \\ 160 \times 10^{-7} f_{\mathrm{v}} {D_{\mathrm{m}}}^3 & \nu n < 2000 \end{cases}, \tag{11}$$

where f_{l} and f_{v} are coefficients corresponding to the bearing design and lubricant type. D_{m} is the bearing's pitch diameter, and $n = \frac{60}{2\pi}|\omega_{\mathrm{i}} - \omega_{\mathrm{o}}|$.

Lubricant's viscosity-temperature relationship can be estimated as [51]

$$\nu = \nu_0 e^{-\beta(T_{\mathrm{L}} - T_{\mathrm{L0}})}, \tag{12}$$

where ν_0 is the initial viscosity at the initial temperature of lubricant T_{L0}.

The heat generation of bearings can be expressed as

$$Q_{\mathrm{gl}} = 10^{-3} |\omega_{\mathrm{i}} - \omega_{\mathrm{o}}| M_{\mathrm{l}}, \tag{13a}$$

$$Q_{\mathrm{gv}} = 10^{-3} |\omega_{\mathrm{i}} - \omega_{\mathrm{o}}| M_{\mathrm{v}}, \tag{13b}$$

$$Q_{\mathrm{g}} = Q_{\mathrm{gl}} + Q_{\mathrm{gv}}, \tag{13c}$$

where Q_{gl} and Q_{gv} are frictional heat from the load and the lubricant, respectively. Q_{g} is in watt.

3.2 Heat dissipation of lubricants

The heat efflux of the system mainly includes the direct heat dissipation during the flow of lubricants and the heat transfer to the environment. The process of heat dissipation of lubricants can be modeled at corresponding nodes (thermal node 63 to 66) and be expressed as

$$Q_{\mathrm{d}} = -\rho_{\mathrm{l}} q_{\mathrm{l}} c_{\mathrm{l}} (T_{\mathrm{L}} - T_{\mathrm{L}\infty}), \tag{14}$$

where q_{l} is the lubricant flow rate of the system, $T_{\mathrm{L}\infty}$ is the lubricant cooling temperature of the system, and the unit of Q_{d} is watt.

3.3 Thermal resistances

Thermal resistances are important to investigate the heat transfer process. For ball bearings, thermal resistances between a single rolling element and rings can be estimated as [52]

$$R^{\mathrm{one}} = \frac{1}{4 k_{\mathrm{Dball}} a} \Psi + \frac{1}{4 k_{\mathrm{Dring}} a} \Psi, \tag{15}$$

where $\Psi = \frac{2}{\pi}K_1(e, \frac{\pi}{2})$, $K_1(e, \frac{\pi}{2})$ and a denotes the elliptical contact area's complete elliptic integral of the first kind and semi-major axis, respectively.

For roller bearings, it can be similarly estimated as

$$R^{\text{one}} = \frac{2a_{\text{roller}}}{\pi k_{\text{Droller}}} f_{\text{rec}}(\varepsilon) + \frac{2a_{\text{roller}}}{\pi k_{\text{Dring}}} f_{\text{rec}}(\varepsilon), \tag{16}$$

where $f_{\text{rec}}(\varepsilon) = \sinh^{-1}\frac{1}{\varepsilon} + \frac{1}{\varepsilon}\sinh^{-1}\varepsilon + \frac{\varepsilon}{3}\left[1 + \frac{1}{\varepsilon^3} - \left(1 + \frac{1}{\varepsilon^2}\right)^{3/2}\right]$, $\varepsilon = \frac{a_{\text{roller}}}{2b}$, a_{roller} is the length of the rectangle contact area, and b is the rectangle contact area's semi-width.

Due to the connection of R^{one} being in parallel, we can obtain equivalent thermal resistances as

$$R_{\text{bi}} = \frac{R_{\text{bi}}^{\text{one}}}{n_b}, \tag{17a}$$

$$R_{\text{bo}} = \frac{R_{\text{bo}}^{\text{one}}}{n_b}, \tag{17b}$$

where n_b denotes the average number of loaded rolling elements.

The system's other thermal resistances can be estimated using the formulas in Table 1. Herein, R_{in} and R_{out} are annular structures' internal and external radius. L denotes the structure's characteristic length. S and A denote the area of heat conduction and heat convection, respectively. Convective heat transfer coefficient h is given by experiments or the Nusselt number Nu in literature. Re denotes the Reynold number. Pr denotes the Prandtl number. Ta denotes the Talyor number. $u_{\text{s}} = \frac{1}{3}\omega_{\text{c}}$ and x is the diameter of bearing housings.

Table 1: Thermal resistances of the system.

Resistance types	Heat conduction
One-dimensional heat conduction	$R = \frac{\ln(R_{\text{out}}/R_{\text{in}})}{2\pi k_{\text{D}} L}$
Flat wall heat conduction	$R = \frac{L}{k_{\text{D}} S}$
Resistance types	**Heat convection $R = \frac{1}{Ah} = \frac{1}{A} \cdot \frac{L}{k_{\text{l}} \cdot Nu}$**
Nu between lubricants and balls [50]	$Nu = 0.33 Re^{0.5} Pr^{0.4}$
Nu between lubricants and cylinders [53]	$Nu = \left(0.35 + 0.34 Re^{0.5} + 0.15 Re^{0.58}\right) Pr^{0.3}$
Nu between lubricants and rings [54]	$Nu = \begin{cases} 2 & Ta < 41 \\ 0.167 Ta^{0.69} Pr^{0.4} & 41 \le Ta < 100 \\ 0.401 Ta^{0.5} Pr^{0.4} & 100 < Ta \end{cases}$
Nu between shafts and ambient [55]	$Nu = \begin{cases} 0.00308 Re + 4.432 & Re < 7300 \\ Re^{0.37} & 7300 \le Re < 9600 \\ 30.5 Re^{-0.0042} & 9600 \le Re \end{cases}$
h between lubricants and inner housing [50]	$h = 0.332 k_{\text{D}} Pr^{1/3} \left(\frac{u_{\text{s}}}{\nu x}\right)^{1/2}$
h between ambient and outer housing [18]	$h = 15\ \text{W}/(\text{m}^2 \cdot \text{K})$

3.4 Heat balance equations

The energy balance principle is used to obtain the system's heat balance equations. With connection to N_j thermal nodes, the pth thermal node's equation

can be expressed as

$$\sum_{j}^{N_j} \frac{T_p - T_j}{R_{p-j}} = Q_p - m_p c_p \frac{\mathrm{d}T_p}{\mathrm{d}t}, \tag{18}$$

where T_p, Q_p, m_p and c_p are the temperature, net heat influx, mass and specific heat capacity of the pth node, respectively.

Note that the heat balance equations should be rewritten into the same form as the motion equations to be suitable for the solving methodology. To better represent TM coupling in the governing equations and analyze nonlinear phenomena in thermal characteristics, we define the generalized thermal damping matrix, generalized thermal stiffness matrix, and generalized nonlinear thermal force matrix in heat balance equations corresponding to their counterparts in motion equations. The temperatures, nonlinear thermal resistances, or nonlinear net heat influx at the corresponding thermal nodes calculate generalized nonlinear thermal forces. Then, the heat balance equations are presented as

$$\mathbf{C}_{\mathrm{T}}\dot{\mathbf{T}} + \mathbf{K}_{\mathrm{T}}\mathbf{T} + \hat{\mathbf{F}}_{\mathrm{T}}(\mathbf{T}) = \mathbf{F}_{\mathrm{T}}, \tag{19}$$

where the temperature vector is $\mathbf{T} = [T_1 \quad T_2 \quad \dots \quad T_p \quad \dots \quad T_n]^{\mathrm{T}}$ $(p = 1 \sim n)$, in which $n = \mathrm{nDoF}_{\mathrm{Thermal}}$ represents the number of thermal DoFs. The generalized thermal damping matrix $\mathbf{C}_{\mathrm{T}}$, generalized thermal stiffness matrix $\mathbf{K}_{\mathrm{T}}$ are given in Appendix C. The generalized nonlinear thermal force matrix $\hat{\mathbf{F}}_{\mathrm{T}}(\mathbf{T})$ consists of generalized nonlinear bearing thermal forces F_{bear} related to $\mathbf{R}_{\mathrm{bear}}$, generalized nonlinear lubricant thermal forces F_{lub} related to $\mathbf{R}_{\mathrm{lub}}$, and generalized nonlinear heat generation/dissipation thermal forces F_{heat} related to Q_{g} and Q_{d}. The thermal constant matrix $\mathbf{F}_{\mathrm{T}}$ consists of the ambient temperature T_∞ and the lubricant cooling temperature $T_{\mathrm{L}\infty}$ with corresponding coefficients.

4 Solving Methodology

The modified IHB method, presented by authors in the previous work [9], enables the simultaneous solution of motion and heat balance equations. Herein, it is utilized to investigate nonlinear characteristics of the coupled TM dual-rotor system. We further divide the preset error tolerance into the dynamic and thermal parts, in accordance with the dimensional differences of vibration responses and temperature variations. It can avoid potential divergence situations and improve the computational efficiency of the governing equations for complex systems with a high DoF.

4.1 Modified IHB method

The method requires a time-scale transform $\tau = \omega_1 t$ as

$$\dot{\mathbf{X}}_{\mathrm{M}} = \frac{\mathrm{d}\mathbf{X}_{\mathrm{M}}}{\mathrm{d}\tau}\frac{\mathrm{d}\tau}{\mathrm{d}t} = \omega_1 \mathbf{X}_{\mathrm{M}}^{'}, \tag{20a}$$

$$\ddot{\mathbf{X}}_{\mathrm{M}} = \frac{\mathrm{d}\dot{\mathbf{X}}_{\mathrm{M}}}{\mathrm{d}\tau}\frac{\mathrm{d}\tau}{\mathrm{d}t} = \omega_1^2 \mathbf{X}_{\mathrm{M}}^{''}, \tag{20b}$$

$$\dot{\mathbf{T}} = \frac{\mathrm{d}\mathbf{T}}{\mathrm{d}\tau}\frac{\mathrm{d}\tau}{\mathrm{d}t} = \omega_1 \mathbf{T}^{'}, \tag{20c}$$

where ($'$) and ($''$) denote derivatives with respect to dimensionless time τ.

Governing equations are obtained by combining the motion equations Eq. (8) with the heat balance equations Eq. (19) simultaneously as

$$\omega_1^2 \mathbf{M}\mathbf{X}^{''} + \omega_1 \mathbf{C}\mathbf{X}^{'} + \mathbf{K}\mathbf{X} + \hat{\mathbf{F}}(\mathbf{X}) = \mathbf{F}(\tau), \tag{21}$$

where $\mathbf{X} = \begin{bmatrix} \mathbf{X}_{\mathrm{M}} \\ \hline \mathbf{T} \end{bmatrix}$, $\mathbf{M} = \left[\begin{array}{c|c} \mathbf{M}_{\mathrm{M}} & \mathbf{0} \\ \hline \end{array}\right]$, $\mathbf{C} = \left[\begin{array}{c|c} \mathbf{C}_{\mathrm{M}} + \Omega\mathbf{J}_{\mathrm{M}} & \\ \hline & \mathbf{C}_{\mathrm{T}} \end{array}\right]$, $\mathbf{K} = \left[\begin{array}{c|c} \mathbf{K}_{\mathrm{M}} & \\ \hline & \mathbf{K}_{\mathrm{T}} \end{array}\right]$, $\hat{\mathbf{F}}(\mathbf{X}) = \begin{bmatrix} \hat{\mathbf{F}}_{\mathrm{M}}(\mathbf{X}) \\ \hline \hat{\mathbf{F}}_{\mathrm{T}}(\mathbf{T}) \end{bmatrix}$, $\mathbf{F}(\tau) = \begin{bmatrix} \mathbf{F}_{\mathrm{M}}(\tau) \\ \hline \mathbf{F}_{\mathrm{T}} \end{bmatrix}$.

Expanding Eq. (21) around a trial solution $\mathbf{X}_0$ using Taylor expansion as

$$\omega_1^2 \mathbf{M}\delta\mathbf{X}^{''} + \omega_1 \mathbf{C}\delta\mathbf{X}^{'} + \mathbf{K}\delta\mathbf{X} + \tilde{\mathbf{F}}(\mathbf{X}_0)\delta\mathbf{X} = \mathbf{r}, \tag{22}$$

where $\delta\mathbf{X} = \mathbf{X} - \mathbf{X}_0$, $\tilde{\mathbf{F}}(\mathbf{X}_0) = \frac{\partial\hat{\mathbf{F}}(\mathbf{X})}{\partial\mathbf{X}}\Big|_{\mathbf{X}=\mathbf{X}_0}$, $\mathbf{r} = \mathbf{F}(\tau) - \omega_1^2\mathbf{M}\mathbf{X}_0^{''} - \omega_1\mathbf{C}\mathbf{X}_0^{'} - \mathbf{K}\mathbf{X}_0 - \hat{\mathbf{F}}(\mathbf{X}_0)$.

According to truncated Fourier series, the periodic solution of the ith DoF can be expressed as

$$\mathbf{X}_i = a_0 + \sum_{j}^{s} (a_j \cos j\pi + b_j \sin j\pi) \quad (i = 1 \sim \mathrm{nDoF}), \tag{23}$$

where s represents the number of periodic solution's truncated harmonic terms, determined by the specific dynamic problems of interest. nDoF denotes the total DoFs of the system ($\mathrm{nDoF} = \mathrm{nDoF}_{\mathrm{Dynamic}} + \mathrm{nDoF}_{\mathrm{Thermal}}$).

Solution vectors $\mathbf{X}$ and $\delta\mathbf{X}$ can be denoted as

$$\mathbf{X} = \mathbf{G}\mathbf{A},\ \delta\mathbf{X} = \mathbf{G}\delta\mathbf{A}, \tag{24}$$

where $\mathbf{G} = \mathrm{diag}\begin{pmatrix} \mathbf{D} & \cdots & \mathbf{D} \end{pmatrix}$, $\mathbf{D} = \begin{pmatrix} 1 & \cos\tau & \cdots & \cos s\tau & \sin\tau & \cdots & \sin s\tau \end{pmatrix}$ denotes the trigonometric basis vector, and $\mathrm{diag}(\cdot)$ denotes diagonal matrix. $\mathbf{A} = \begin{bmatrix} \mathbf{A}_1 & \cdots & \mathbf{A}_i & \cdots & \mathbf{A}_{\mathrm{nDoF}} \end{bmatrix}^{\mathrm{T}}$, $\delta\mathbf{A} = \begin{bmatrix} \delta\mathbf{A}_1 & \cdots & \delta\mathbf{A}_i & \cdots & \delta\mathbf{A}_{\mathrm{nDoF}} \end{bmatrix}^{\mathrm{T}}$ denotes the Fourier coefficient matrices, where $\mathbf{A}_i = \begin{bmatrix} a_0 & a_1 & \cdots & a_s & b_1 & \cdots & b_s \end{bmatrix}_i^{\mathrm{T}}$.

Substituting Eq. (24) into Eq. (22), we can transform the incremental equations into the algebraic equations

$$\mathbf{J}\delta\mathbf{A} = \mathbf{R}. \tag{25}$$

The residual vector's modified solution procedure is given as

$$\mathbf{R} = \frac{1}{\pi}\int_0^{2\pi} \mathbf{G}^{\mathrm{T}}\mathbf{G}\mathrm{d}\tau\boldsymbol{\eta}^{\mathbf{r}}, \tag{26}$$

where $\frac{1}{\pi}\int_0^{2\pi} \mathbf{G}^{\mathrm{T}}\mathbf{G}\mathrm{d}\tau$ is a constant matrix. $\boldsymbol{\eta}^{\mathbf{r}}$ denotes the Fourier coefficient matrix of $\mathbf{r}$.

Jacobian matrix is defined as $\mathbf{J} = \mathbf{J}_0 + \tilde{\mathbf{J}}$. The linear part's modified solution procedure is given as

$$\mathbf{J}_0 = \frac{1}{\pi}\omega_1^2\int_0^{2\pi} \mathbf{D}^{\mathrm{T}}\mathbf{D}^{''}\mathrm{d}\tau \otimes \mathbf{M} + \frac{1}{\pi}\omega_1\int_0^{2\pi} \mathbf{D}^{\mathrm{T}}\mathbf{D}^{'}\mathrm{d}\tau \otimes \mathbf{C} + \frac{1}{\pi}\int_0^{2\pi} \mathbf{D}^{\mathrm{T}}\mathbf{D}\mathrm{d}\tau \otimes \mathbf{K}, \tag{27}$$

where $\otimes$ is the Kronecker product operator. $\frac{1}{\pi}\int_0^{2\pi} \mathbf{D}^{\mathrm{T}}\mathbf{D}^{''}\mathrm{d}\tau$ and $\frac{1}{\pi}\int_0^{2\pi} \mathbf{D}^{\mathrm{T}}\mathbf{D}^{'}\mathrm{d}\tau$ are constant matrices.

The nonlinear part's modified solution procedure is given as

$$\tilde{\mathbf{J}} = \frac{1}{\pi}\int_0^{2\pi} \mathbf{G}^{\mathrm{T}}(\mathbf{H}\boldsymbol{\eta}^{\tilde{\mathbf{F}}})\mathbf{G}\mathrm{d}\tau = \mathbf{S}\boldsymbol{\eta}^{\tilde{\mathbf{F}}}, \tag{28}$$

where $\mathbf{S} = \frac{1}{\pi}\int_0^{2\pi} \mathbf{D}^{\mathrm{T}}\mathbf{D} \otimes \mathbf{E}\mathrm{d}\tau$ is obtained using fast Fourier transformation (FFT). $\boldsymbol{\eta}^{\tilde{\mathbf{F}}}$ denotes the Fourier coefficient matrix of $\tilde{\mathbf{F}}$ and obtained using the discrete Fourier transform (DFT) and the inverse Fourier transform (IDFT).

Substituting the trial solution $\mathbf{X}_0 = \mathbf{G}\mathbf{A}_0$ to Eq. (25), we can obtain the first iteration solutions and continually update the Newton-Raphson iterative procedure

$$\delta\mathbf{A}^{(k)} = \mathbf{J}^{-1}\mathbf{R},\ \mathbf{A}^{(k+1)} = \mathbf{A}^{(k)} + \delta\mathbf{A}^{(k)},\ \mathbf{X}^{(k+1)} = \mathbf{G}\mathbf{A}^{(k+1)}, \tag{29}$$

until the residual vector norms of the dynamic and thermal part are less than the preset dynamic and thermal error tolerance, respectively. Upon convergence, the periodic solution of Eq. (21) is given by $\mathbf{X} = \mathbf{G}\mathbf{A}$.

Herein, the preset error tolerance of the dynamic part is 10^{-8}, and the thermal part is 10^{-3}.

4.2 Floquet theory

We utilize the Floquet theory, a stability discrimination method, to investigate the stability evolution and bifurcation characteristics of the system's nonlinear phenomena.

The incremental equations Eq. (22) can be rewritten as

$$\mathbf{H}^{'} = \mathbf{B}(\tau)\mathbf{H}, \tag{30}$$

where $\mathbf{H} = \begin{bmatrix} \delta\mathbf{X} & \delta\mathbf{X}^{'} \end{bmatrix}^{\mathrm{T}}$. $\mathbf{B}(\tau)$ is the state matrix and reflects the connection between the variable vector and its derivative vector.

According to the Floquet theory, the transition matrix can be defined as

$$\mathbf{E} = \int_0^{2\pi} e^{\mathbf{B}(\tau)\tau} \mathrm{d}\tau. \tag{31}$$

As it is impossible to analytically obtain the transition matrix for rotor systems modeled by several DoFs [56, 57], we apply the single-iteration pass (SIP) algorithm to evaluate the transition matrix. For the SIP algorithm, the transition matrix can be estimated by dividing numerous equal intervals in a period (each interval should be sufficiently small). Hence, a period T is divided into N_k intervals denoted by τ_k. In the kth interval ($\Delta_k = \tau_k - \tau_{k-1}$), the state matrix $\mathbf{B}(\tau)$ can be replaced by $\mathbf{B}_k$ and expressed as

$$\mathbf{B}_k = \frac{1}{\Delta_k} \int_{\tau_{k-1}}^{\tau_k} \mathbf{B}(\zeta) \mathrm{d}\zeta. \tag{32}$$

Then, the approximate transition matrix can be obtained by

$$\mathbf{E}_{\mathrm{SIP}} = \prod_{k=1}^{N_k} \left(\mathbf{I} + \sum_{i=1}^{N_i} \frac{(\Delta_k \mathbf{B}_k)^i}{i!} \right). \tag{33}$$

Based on the relationship between the eigenvalues of the transition matrix and the unit circle in the complex plane, the stability and bifurcation characteristics of each periodic solution can be analyzed as follows:

- If all eigenvalues are inside the unit circle, the periodic solution is stable. Otherwise, it is unstable.
- If an eigenvalue crosses the unit circle from the positive real number $+1$, there exists a transcritical, symmetry-breaking, or saddle-node bifurcation.
- If an eigenvalue crosses the unit circle from the negative real number -1, there exists a period-doubling bifurcation.
- If a pair of eigenvalues crosses the unit circle from elsewhere, there exists a Neimark-Sacker bifurcation.

5 Results and discussion

This section demonstrates and analyzes the evolution of the nonlinear dynamic and thermal characteristics of the dual-rotor system as the TM coupling degree increases. By setting different lubricant flow rates q_{l} to control the heat dissipation of the system, five TM coupling degrees are simulated as: the lowest, low, medium, high and highest TM coupling degrees with $q_{\mathrm{l}} = 20$ L/min, $q_{\mathrm{l}} = 10$ L/min, $q_{\mathrm{l}} = 5$ L/min, $q_{\mathrm{l}} = 2$ L/min and $q_{\mathrm{l}} = 1$ L/min, respectively. Unless otherwise specified, the ambient temperature and the lubricant cooling temperature are both 25 °C. Generalized nonlinear thermal forces are further shown to investigate the nonlinearity sources in thermal characteristics. The effect of global temperature increase is also investigated by nonlinear characteristic analysis with a lower lubricant cooling temperature.

5.1 Selections and convergence analysis of truncated harmonic terms

The truncation of harmonic terms is a crucial step in applying the modified IHB method to solve governing equations, as it significantly impacts the accuracy of the results. To address this, we compared the results obtained by setting the truncation of harmonic terms from the first-order up to the fourth-order. Steady-state temperatures after heat balance can be represented by the direct-current component of harmonic terms. Vibration responses are mainly excited by $\mathbf{F}(\tau)$. The nonlinear characteristics of the primary resonance regions are the focus of our study. Therefore, the frequency components are set as $\frac{\omega_1}{2}$, $\frac{\lambda\omega_1}{2}$, ω_1, $\lambda\omega_1$ in the case of the first-order truncated harmonic. For the kth-order truncated harmonic, the frequency components range from $\frac{\omega_1}{2}$ to $k\lambda\omega_1$, and the trigonometric basis vector $\mathbf{D}$ can be set as

$$\mathbf{D} = \begin{pmatrix} 1 & \cos\frac{1}{2}\tau & \cos\frac{\lambda}{2}\tau & \cos\tau & \cos\lambda\tau & \cos 2\tau & \cos 2\lambda\tau & \cdots & \cos k\tau & \cos k\lambda\tau \\ & \sin\frac{1}{2}\tau & \sin\frac{\lambda}{2}\tau & \sin\tau & \sin\lambda\tau & \sin 2\tau & \sin 2\lambda\tau & \cdots & \sin k\tau & \sin k\lambda\tau \end{pmatrix}. \tag{34}$$

Fig. 5 shows the comparisons of the amplitude-frequency responses and the temperature variations among different truncated harmonic terms. We select the 3# inter-shaft roller bearing (dynamic node 8 in Fig. 5(a) and thermal node 58 of its rolling elements in Fig. 5(c)) and the HPC disk (dynamic node 14 in Fig. 5(b) and thermal node 41 in Fig. 5(d)) as representative positions for the system.

The vibration response amplitudes of the dynamic nodes are denoted as

$$\text{Amplitude} = \sqrt{\frac{\int_0^T \left((x(t)-\bar{x})^2 + (y(t)-\bar{y})^2\right) \mathrm{d}t}{T}}, \tag{35}$$

where $\bar{x}$ and $\bar{y}$ are average vertical and horizontal displacements in a time period T, respectively. It can be found that the vibration responses and temperatures obtained by the first- and second-order truncated harmonics at the resonant peaks are larger than those in the other two cases. To further analyze the convergence of truncated harmonic terms, the four sets of points, A, B, C, and D, corresponding to four different speeds, $\omega = 400$ rad/s, $\omega = 484$ rad/s, $\omega = 530$ rad/s and $\omega = 584$ rad/s, are set, respectively. Fig. 6 presents the residual comparisons of the governing equations among four selections of truncated harmonic terms.

The residuals of the governing equations are calculated as

$$\text{Residual} = \mathbf{F}(\tau) - \omega_1^2\mathbf{M}\mathbf{X}^{''} - \omega_1\mathbf{C}\mathbf{X}^{'} - \mathbf{K}\mathbf{X} - \hat{\mathbf{F}}(\mathbf{X}). \tag{36}$$

As shown in Fig. 6, it can be observed that for the HPC disk, regardless of whether the rotation speed is near the resonant peaks, the residuals of the motion equations and heat balance equations always remain at a relatively small

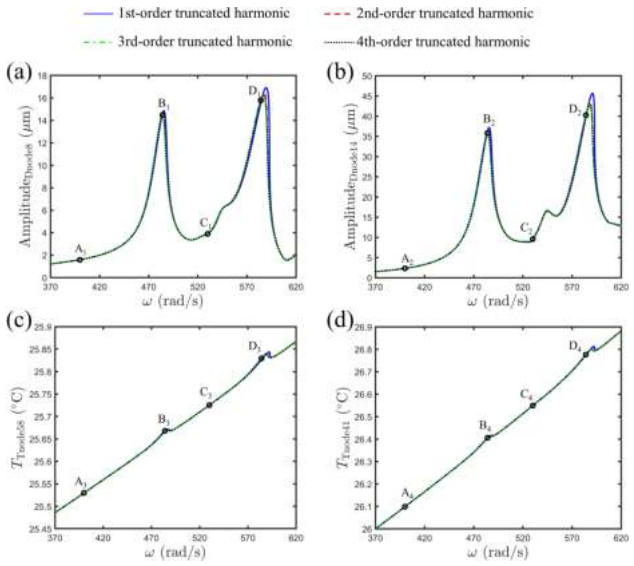

Figure 5: Result comparisons among four selections of truncated harmonic terms. (a) and (b) Amplitude-frequency responses of the dynamic node 8 and 14. (c) and (d) Temperature variations of the thermal node 58 and 41.

magnitude. It indicates that setting higher-order truncated harmonics offers very limited improvement in accuracy. However, for the 3# inter-shaft bearing, the equations exhibit larger residuals near the resonant peak. Specifically, for points B_1, B_3, D_1, and D_3, the residual magnitude significantly decreases as the order of truncated harmonics increases, converging at the third-order harmonic. Considering both computational accuracy and efficiency, subsequent results are calculated using the third-order truncated harmonic.

On the other hand, by comparing the equation residuals at the two positions, the 3# inter-shaft bearing and the HPC disk, it can be found that the residuals for the 3# inter-shaft bearing are consistently many orders of magnitude larger than those for the HPC disk. This is because the system experiences greater nonlinear forces at this position. Fig. 7 shows part of the nonlinear forces of the 3# roller bearing, which includes time-varying and average radial bearing loads and generalized nonlinear heat generation thermal forces. Since the nonlinear forces are more than two orders of magnitude larger than the corresponding residuals, these results can be considered acceptable for the dynamic node 8 and the thermal node 58.

5.2 Nonlinear dynamic characteristic analysis

The eccentricity excitation forces of the LP rotor and the HP rotor are the main reasons for the resonances of the system. The 3# inter-shaft roller bearing connects the LP rotor and the HP rotor, and its inner ring is located at the

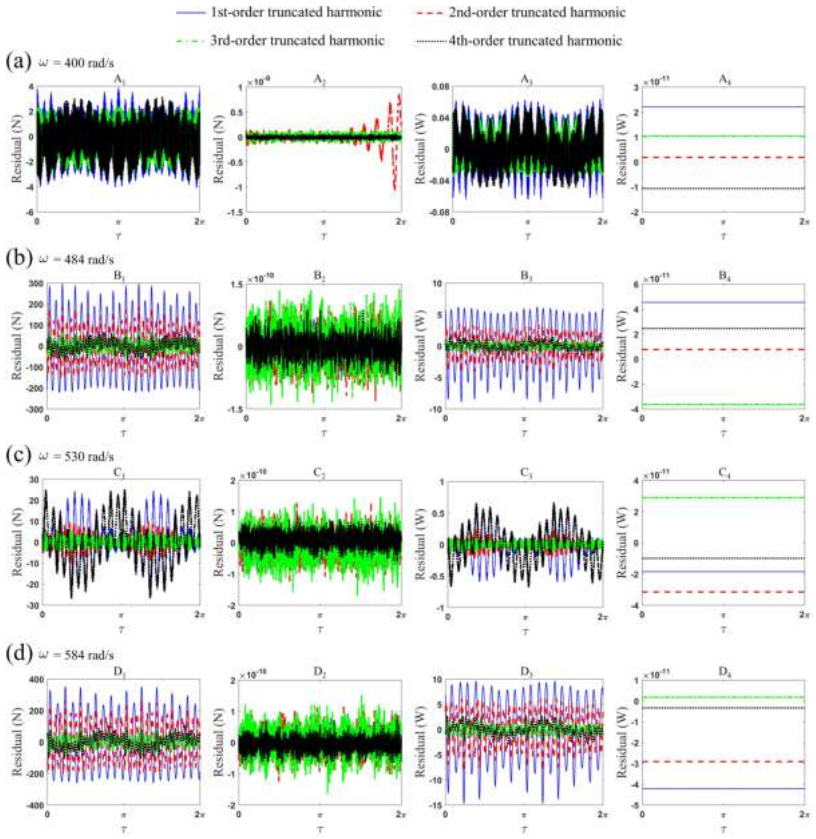

Figure 6: Residual comparisons of the governing equations among four selections of truncated harmonic terms. (a) A_1, A_2, A_3 and A_4 at $\omega = 400$ rad/s. (b) B_1, B_2, B_3 and B_4 at $\omega = 484$ rad/s. (c) C_1, C_2, C_3 and C_4 at $\omega = 530$ rad/s. (d) D_1, D_2, D_3 and D_4 at $\omega = 584$ rad/s.

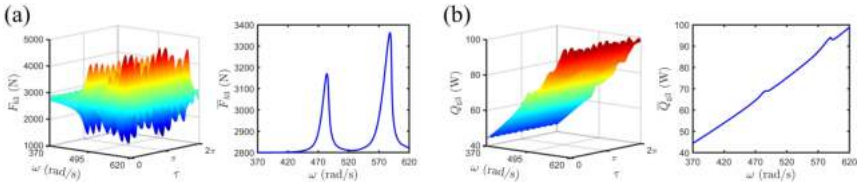

Figure 7: Part of the nonlinear forces of the 3# roller bearing. (a) Time-varying and average radial bearing loads at the dynamic node 8. (b) Time-varying and average generalized nonlinear heat generation thermal forces at the thermal node 58.

dynamic node 8, resulting in more significant variations in vibration responses at this position. Therefore, we select the amplitude-frequency response of the dynamic node 8 as the representative of all dynamic nodes, to perform a more comprehensive analysis of the nonlinear dynamic characteristics. In order to facilitate subsequent analysis, we define δ_{vk}, u_{bk}, u_{ik}, u_{ok} to represent the radial expansion of rolling elements of the kth bearing, where $k = 1, 2, 3, 4$ corresponds to the bearing number.

Let us start the nonlinear dynamic characteristic analysis from the lowest, low, and medium TM coupling degrees with $q_l = 20$ L/min, $q_l = 10$ L/min and $q_l = 5$ L/min. Fig. 8(a) shows there are two resonant peaks (RP) in the amplitude-frequency response curves. As the lubricant flow rate decreases, the resonant peaks shift towards lower frequencies, and the amplitudes of the vibration responses become larger. From Fig. 8(b), it can be found the relationship among the RC variations is $\delta_{v4} > \delta_{v3} > \delta_{v1} > \delta_{v2}$ for the lowest TM coupling degree. The absolute values are all within 1 μm, which means that the thermal characteristics have little effect on the dynamic characteristics. Particularly, the RC variations of the 1# ball bearing and 2# ball bearing are still negative and decrease with rotation speed increase. The situations are opposite for the 3# roller bearing and 4# roller bearing, which is more in line with our understanding from previous work. In the case of low TM coupling degree, the relationship among the RC variations is $\delta_{v4} > \delta_{v3} > \delta_{v2} > \delta_{v1}$. δ_{v1} and δ_{v2} gradually increase as the rotation speed increases, and the value of δ_{v2} changes from negative to positive. Continuing to decrease the lubricant flow rate to $q_l =$ 5 L/min, the relationship among the RC variations has become $\delta_{v4} > \delta_{v2} > \delta_{v1} > \delta_{v3}$. In this case, the effective RCs of all bearings become larger, equivalent to reducing the stiffness of the bearings.

Fig. 9 shows the nonlinear dynamic characteristics of the system under the high TM degree. Two bifurcation points (BP) first emerge in Fig. 9(a). BP_1 represents the periodic solution where the system transitions from a stable state (the blue solid line) to an unstable state (the red solid line). Conversely, BP_2 represents the periodic solution where the system transitions from an unstable state to a stable state. In Fig. 9(c), the blue dot represents the start rotation speed, and the red dot represents the end rotation speed. The gradient color from blue to red represents the direction of the eigenvalue crossing the unit circle. According to the Floquet theory, BP_1 and BP_2 are both saddle-node bifurcation points. A resonance hysteresis phenomenon and a bi-stable interval are manifested between the rotation speed range corresponding to the two adjacent bifurcation points. The reason for emerging with the nonlinear phenomenon is that the effective RCs increase rapidly, even more than five times the initial RCs of the 2# and 4# bearing at $\omega = 620$ rad/s (see Fig. 9(b)). The relationship among the RC variations remains constant, staying at $\delta_{v4} > \delta_{v2} > \delta_{v1} > \delta_{v3}$. δ_{v1} and δ_{v2} move closer to δ_{v4}, and gradually away from δ_{v3} compared with the case of Fig. 8(b).

In the case of $q_l = 1$ L/min, the nonlinear dynamic characteristics for the highest TM coupling degree undergo further drastic changes, as shown in Fig. 10. Compared with the case of $q_l = 2$ L/min, there first emerges two saddle-

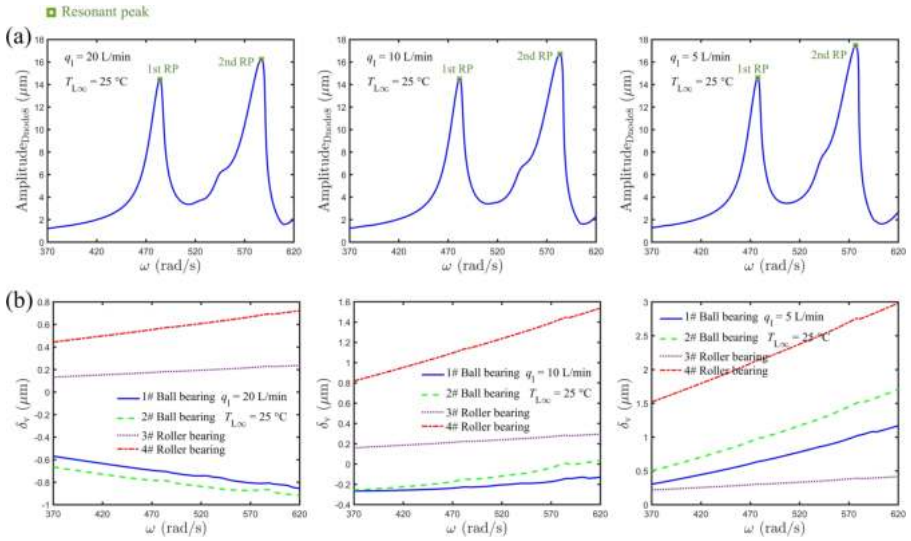

Figure 8: Nonlinear dynamic characteristics under the lowest, low and medium TM coupling degrees with q_l = 20 L/min, q_l = 10 L/min and q_l = 5 L/min, respectively. (a) Amplitude-frequency response of the dynamic node 8. (b) RC variations of the four bearings.

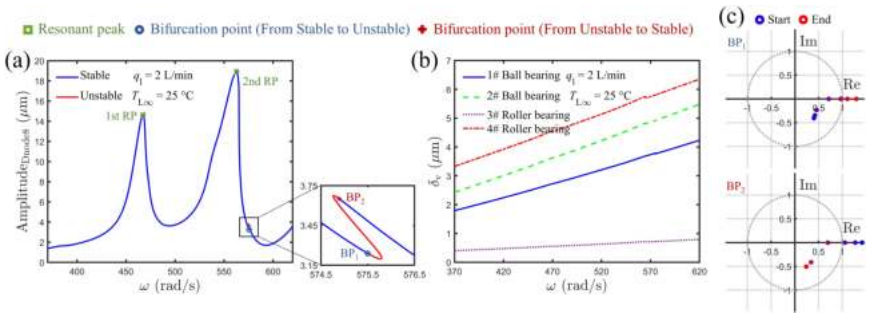

Figure 9: Nonlinear dynamic characteristics under the high TM coupling degree with q_l = 2 L/min. (a) Amplitude-frequency response of the dynamic node 8. (The blue solid line represents the stable solution, and the red solid line represents the unstable solution). (b) RC variations of the four bearings. (c) Relationships between the eigenvalues and the unit circle of the bifurcation points.

node bifurcation points BP_1 and BP_2 near the 2nd RP and exhibits a small resonance hysteresis phenomenon. The saddle-node bifurcation points in Fig. 9(a) evolve into Neimark-Sacker bifurcation points BP_3 and BP_4 according to the manner in which their eigenvalues cross the unit circle (see Fig. 10(c)). It transforms the bi-stable region to the unstable region with higher vibration response amplitudes than the value of the resonant peak. From Fig. 10(b) and Fig. 9(b), it can be found that the effective RCs of the bearings are nearly twice as much. The RC variation velocity of the 2# ball bearing continues to rise with the increase in coupling degree, eventually surpassing the 4# ball bearing.

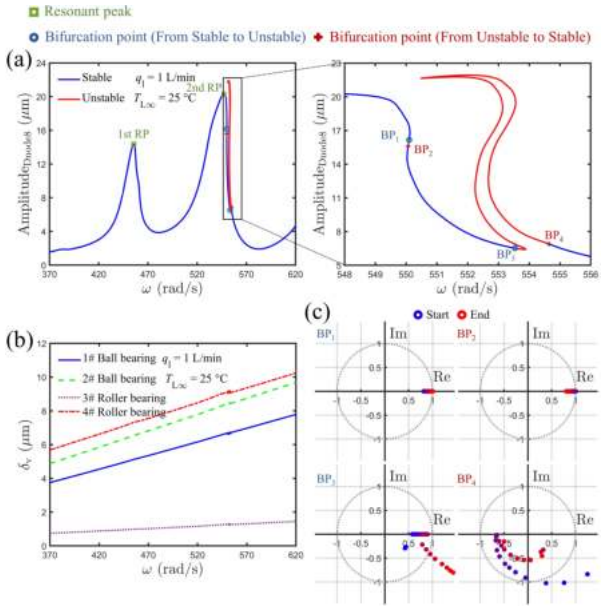

Figure 10: Nonlinear dynamic characteristics under the highest TM coupling degree with $q_l = 1$ L/min. (a) Amplitude-frequency response of the dynamic node 8. (The blue solid line represents the stable solution, and the red solid line represents the unstable solution). (b) RC variations of the four bearings. (c) Relationships between the eigenvalues and the unit circle of the bifurcation points.

Particularly, Fig. 11 shows the amplitude-frequency responses of 1# ball bearing (dynamic node 1). Due to its special position within the system, its nonlinear dynamic characteristics exhibit more significant changes as the TM coupling degree increases. The bi-stable interval in Fig. 11(a) has a larger and broader range of amplitude variations compared to Fig. 9(a). In the case of q_l = 1 L/min, the amplitude of the unstable region at $[\omega_{BP_3}, \omega_{BP_4}]$ penetrates the stable region at $[\omega_{BP_2}, \omega_{BP_3}]$, transforming the resonance hysteresis phenomenon into the looping phenomena in Fig. 11(b).

Fig. 12 shows the orbits and vibration modes (the zigzag lines go through

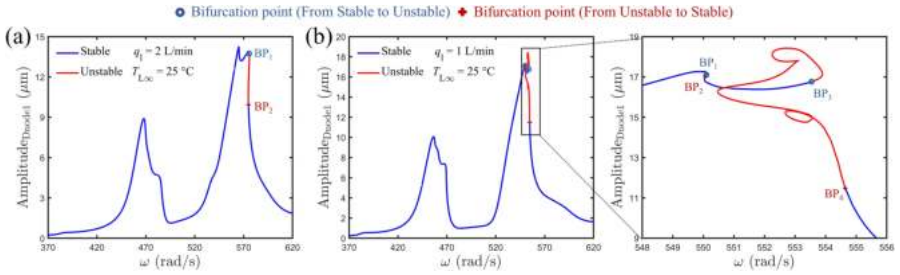

Figure 11: Amplitude-frequency responses of the dynamic node 1 (a) under the high TM coupling degree with $q_l = 2$ L/min. (b) under the highest TM coupling degree with $q_l = 1$ L/min. (The blue solid line represents the stable solution, and the red solid line represents the unstable solution).

the orbits) of the LP rotor and HP rotor at the primary resonant peaks under different TM coupling degrees. The black upper and lower triangles denote the locations of the bearings. Due to the consideration of the gravity of the rotors, the overall vibration response is negative. The HP rotor has the same vibration modes as the LP rotor behind the linear elastic support (dynamic node 4 to 11) because of the influence of the inter-shaft bearing force. As the TM coupling degree increases, the system's vibrations become more intense, and the dynamic nodes' orbits exhibit different degrees of distortion.

As discussed earlier, the RC variations of four bearings can be diverse under different lubricant flow rates. However, the relationship among the radial expansion of the rolling elements, the inner ring and the outer ring of each bearing is still ordered as $u_o > u_i > u_b$, as shown in Fig. 13. When the radial expansion of the outer ring is not large enough, resulting in it being less than the sum of the radial expansion of the rolling elements and the inner ring (see Fig. 13(a)), the bearings' RC will manifest as a negative value. Furthermore, this difference is amplified with the increasing rotation speed, as exhibited in Fig. 8(b). In Fig. 13(b) and Fig. 13(c), the decrease of the lubricant flow rate rapidly increases the radial expansion of every bearing component, with the outer ring experiencing the fastest growth.

Fig. 8-13 show the nonlinear dynamic characteristic evolution of the dual-rotor system under different TM coupling degrees. It can be found that the higher TM coupling degree will shift the primary resonance regions into a lower frequency direction and induce larger vibration responses. On the other hand, as the TM coupling degree increase, the dual-rotor system will emerge with more bifurcation points and an increased number of, as well as larger, unstable regions. Sometimes, saddle-node bifurcation points can even transform into Neimark-Sacker bifurcation points, leading the resonance hysteresis phenomena to more complex nonlinear phenomena. We know that the fundamental reason for coupled TM effects on the nonlinear dynamic characteristics is the continuous variation of the effective RC of the bearing with rotation speed. The

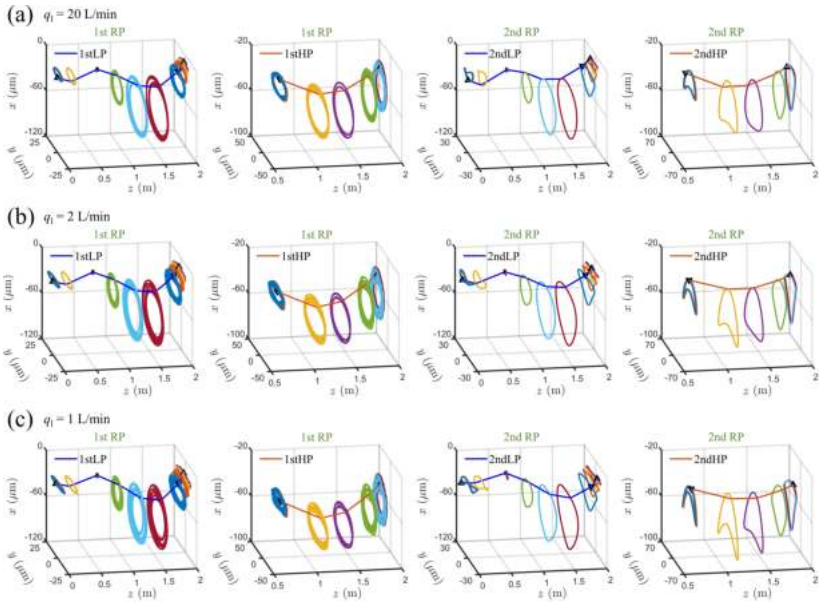

Figure 12: Orbits and vibration modes of the LP rotor and HP rotor at the primary resonant peaks (a-c) under the lowest, high, and highest TM coupling degrees with $q_l = 20$ L/min, $q_l = 2$ L/min, and $q_l = 1$ L/min, respectively.

relationship among the RC variations for the four bearings shows that it is not fixed when the TM coupling degree is not high enough. In the case of sufficient lubricant flow rate, the relationship is related to the sensitivity of the bearing to heat variation of the system, which is dependent on the structure parameters, material parameters, and temperatures of bearing components. It is worth mentioning that δ_v fluctuates and can even be negative and decrease with rotation speed increase, which does not necessarily have a higher value in the high rotation speed range or resonant peaks. In the case of insufficient lubricant flow rate, the relationship among the RC variations stabilizes at the order as $\delta_{v4} > \delta_{v2} > \delta_{v1} > \delta_{v3}$, and δ_v no longer fluctuates arbitrarily. This is because the TM coupling degree is high enough, and the temperatures of bearing components become the dominant determining factor in δ_v. Understanding the evolution patterns of the effective RCs, with the increase in TM coupling degrees, can help determine appropriate lubricant flow rates and safe temperature ranges for the system, to avoid setting operating speeds in unstable regions.

5.3 Nonlinear thermal characteristic analysis

Before analyzing the nonlinear thermal characteristics of the system, the overall temperature variations of thermal nodes with rotation speed are demonstrated in Fig. 14. The maximum value of the temperature at each rotation speed

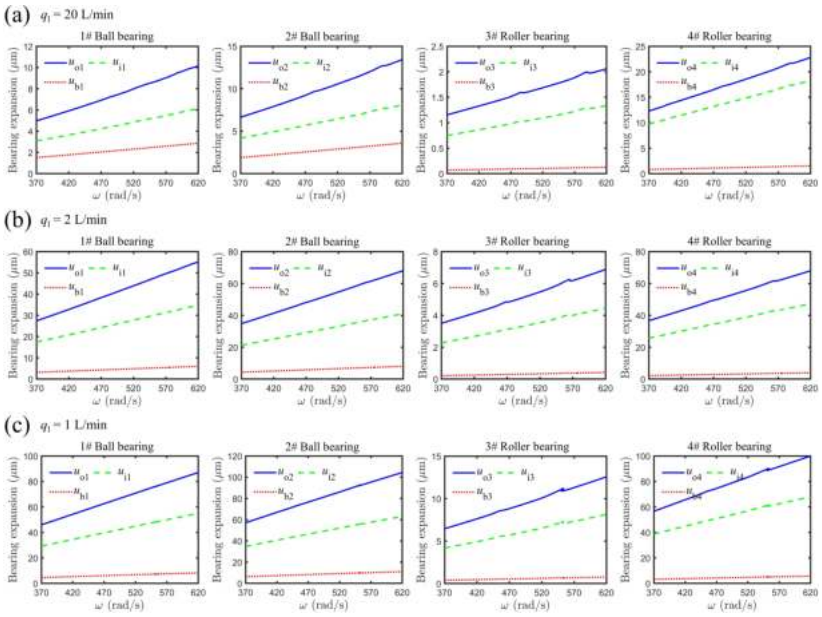

Figure 13: Radial expansion of the rolling elements, the inner ring and the outer ring of the four bearings (a-c) under the lowest, high, and highest TM coupling degrees with $q_l = 20$ L/min, $q_l = 2$ L/min, and $q_l = 1$ L/min, respectively.

(including bi-stable regions) is presented in Fig. 14(a) and Fig. 14(b). With the decrease of lubricant flow rate, the maximum temperature of the system increases sharply and many thermal nodes have larger temperature variations. Temperature variations of the four bearings with rotation speed are presented in Fig. 14(c), which have significant nonlinear phenomena in accordance with the nonlinear dynamic characteristics (see black square parts). The relationship is $T_{\mathrm{b}} > T_{\mathrm{i}} > T_{\mathrm{o}}$ for the 1# and 2# ball bearings. On the other hand, T_{b}, T_{i} and T_{o} of the 3# and 4# roller bearings are very close.

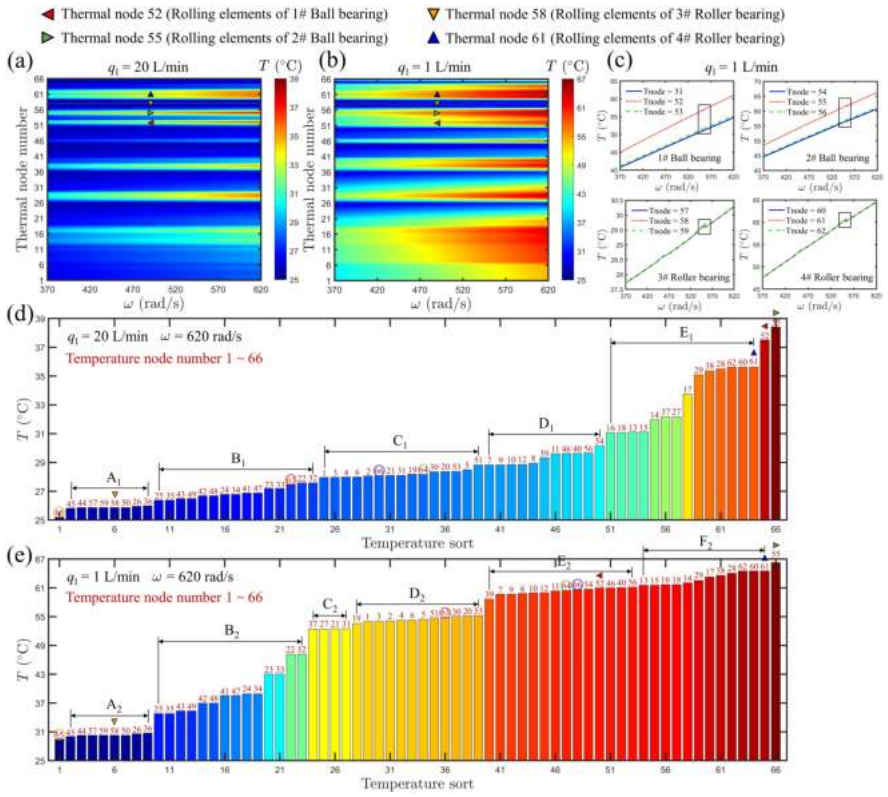

Figure 14: Overall temperature variations of thermal nodes with rotation speed (a) under the lowest TM coupling degree with $q_{\mathrm{l}} = 20$ L/min. (b) under the highest TM coupling degree with $q_{\mathrm{l}} = 1$ L/min. (c) Temperature variations of the four bearings with $q_{\mathrm{l}} = 1$ L/min. (d) Temperature sort of thermal nodes at $\omega = 620$ rad/s with $q_{\mathrm{l}} = 20$ L/min. (e) Temperature sort of thermal nodes at $\omega = 620$ rad/s with $q_{\mathrm{l}} = 1$ L/min.

To analyze the temperature relationships among various thermal nodes and assess the effects of lubricant flow rate on the temperature of thermal nodes in detail, Fig. 14(d) and Fig. 14(e) show temperature sorts of thermal nodes at $\omega = 620$ rad/s with $q_{\mathrm{l}} = 20$ L/min and $q_{\mathrm{l}} = 1$ L/min. Red numbers represent

thermal node numbers. According to the positions of thermal nodes and their temperature, the thermal sorts can be divided into five parts named $A_1 \sim E_1$ from low to high temperature for $q_l = 20$ L/min, and six parts named $A_2 \sim F_2$ from low to high temperature for $q_l = 1$ L/min. From Fig. 14(d), it can be found that the rolling elements of the 2# ball bearing (thermal node 55) have the highest temperature, and the rolling elements of the 1# ball bearing (thermal node 52) has the second highest temperature. The lubricant temperature of the 3# roller bearing (thermal node 65) has the lowest temperature. Part A_1 includes the inner ring, outer ring, and assembly parts of the 3# roller bearing. Part B_1 includes the lubricant of the 1# ball bearing (thermal node 63), the HPC disk, the HPT disk, as well as the midsection of the LP and the HP shafts. Part C_1 includes the lubricants of the 4# roller bearing (thermal node 66) and the 2# ball bearing (thermal node 64), the LPC disk, as well as the inner ring, outer ring and assembly parts of the 1# ball bearing. Part D_1 includes the inner ring, outer ring, and assembly parts of the 2# ball bearing. Part E_1 includes the LPT disk, as well as the inner ring, outer ring, and assembly parts of the 4# roller bearing.

In summary, the relationship among the temperatures of the system can be ordered as 4# roller bearing position (E_1) > 2# ball bearing position (D_1) > 1# ball bearing position (C_1) > most part of the LP and the HP shafts (B_1) > 3# roller bearing position (A_1) in the case of $q_l = 20$ L/min. On the other hand, the relationship among the temperatures of the rolling elements of the bearings is 2# ball bearing > 1# ball bearing > 4# roller bearing > 3# roller bearing. The relationship among the temperatures of the lubricants of the bearings is 2# ball bearing > 4# roller bearing > 1# ball bearing > 3# roller bearing.

For $q_l = 1$ L/min in Fig. 14(e), the highest and the lowest temperatures occur at the same thermal nodes compared with Fig. 14(d). There have been some changes in the relationship among the temperatures of the system as 4# roller bearing position (F_2) > 2# ball bearing position (E_2) > 1# ball bearing position (D_2) > LPC disk and LPT disk position (C_2) > most part of the LP and the HP shafts (B_2) > 3# roller bearing position (A_2). The relationship among the temperatures of the rolling elements of the bearings is 2# ball bearing > 4# roller bearing > 1# ball bearing > 3# roller bearing. The relationship among the temperatures of the lubricants of the bearings is 4# roller bearing > 2# ball bearing > 1# ball bearing > 3# roller bearing. The main effects of the lubricant flow rate decrease on the system temperature can be summarized as (1) The temperature of the LPC disk becomes higher than that of the 1# ball bearing position, the temperature of the LPT disk becomes lower than that of the 4# roller bearing position. They constitute a new part C_2. (2) Temperature rises of the 4# roller bearing position and 2# ball bearing position are apparently higher than that of the 1# ball bearing position and 3# roller bearing position. This influence is also reflected in the rise of δ_v according to Fig. 8(b) and Fig. 10(b). (3) The temperature of rolling elements of the 4# roller bearing becomes higher than that of the 1# ball bearing.

According to the above analysis, it can be inferred that the 4# roller bearing needs an independent lubricant inlet channel with the maximum lubricant flow

rate. In contrast, the 3# roller bearing needs an independent lubricant inlet channel with the minimum lubricant flow rate if the lubricant flow rate for each bearing can be variable. It can distribute lubricant more reasonably and suppress the temperature increase of the system, to avoid the occurrence of more complex nonlinear dynamic characteristics.

Nonlinear temperature variations of the thermal node 58 under different TM coupling degrees are demonstrated in Fig. 15. Comparing Fig. 15(b) with Fig. 9(a), BP_1 has a higher temperature and a lower vibration response amplitude than that of BP_2. However, the entire temperature variation curves show the same bifurcation points and hysteresis phenomena at corresponding rotation speeds.

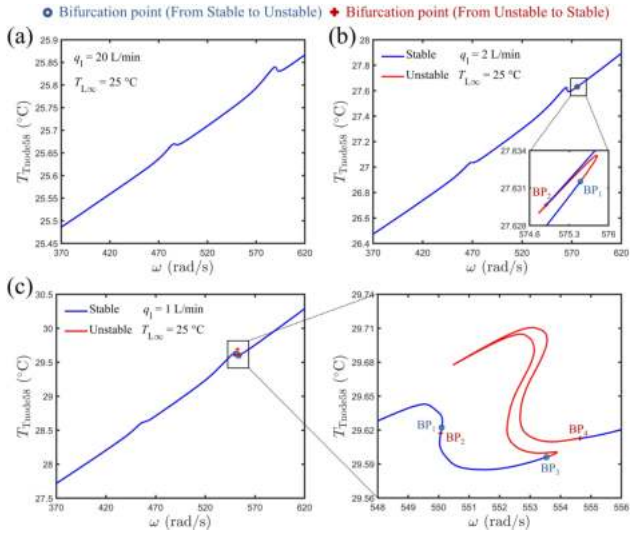

Figure 15: Nonlinear temperature variations at the thermal node 58 (a-c) under the lowest, high, and highest TM coupling degrees with q_l = 20 L/min, q_l = 2 L/min, and q_l = 1 L/min, respectively. (The blue solid line represents the stable solution, and the red solid line represents the unstable solution).

According to Eq. (19), the generalized nonlinear thermal force matrix $\hat{\mathbf{F}}_T(\mathbf{T})$ is an important component of the heat balance equations. It can be inferred that the nonlinear phenomena in temperature variations result from the joint effects of generalized nonlinear bearing, lubricant, and heat generation/dissipation thermal forces. Fig. 16-20 demonstrate time-varying and average nonlinear forces for the highest TM coupling degree with q_l = 1 L/min to detect nonlinearity sources in thermal characteristics. For example, time-varying and average radial bearing loads with rotation speed are shown in Fig. 16. We define F_{bk} to represent the time-varying radial loads of the kth bearing, and $\bar{F}_{bk}$ to represent the average radial loads of the kth bearing, where k = 1, 2, 3, 4 corresponds to the bearing number. The definition rule remains the same and is not specifically

mentioned in the following descriptions.

From Fig. 16, it can be found that the radial bearing loads vary significantly with time at each rotation speed in time-varying results. The nonlinear phenomena of radial bearing loads are shown in average results, which increase sharply at resonant peaks, corresponding to the amplitude of the vibration responses. The 1# ball bearing has the lowest radial loads and the most different looping phenomenon among the four bearings. It is a special case because there is a linear support at the dynamic node 3, and the local structure reduces the radial bearing load of the 1# ball bearing. The 3# roller bearing has the same radial load variations as the 2# ball bearing and the 4# roller bearing because it is an inter-shaft bearing. For more accurate coupled TM results, the time-varying characteristics should be considered in the calculation procedures of bearing thermal resistances and the frictional heat from the load. Therefore, the nonlinear characteristics are also transferred into generalized nonlinear bearing thermal forces (see Fig. 17).

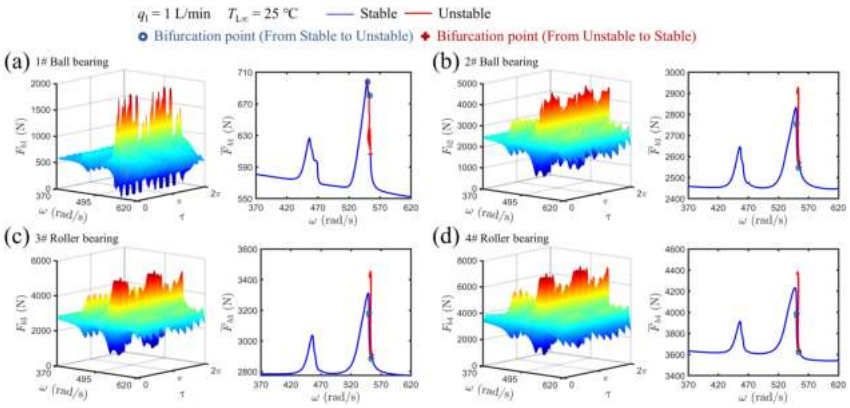

Figure 16: Time-varying and average radial bearing loads (a-d) of the 1# ball bearing, 2# ball bearing, 3# roller bearing and 4# roller bearing, respectively. (The blue solid line represents the stable solution, and the red solid line represents the unstable solution).

Time-varying and average generalized nonlinear bearing thermal forces of the 2# ball bearing and the 3# roller bearing are demonstrated in Fig. 17. Taking the 2# ball bearing as an example, there are $F_{\mathrm{bearo2}} = \frac{T_{\mathrm{o2}} - T_{\mathrm{b2}}}{R_{\mathrm{bo2}}}$, $F_{\mathrm{beari2}} = \frac{T_{\mathrm{i2}} - T_{\mathrm{b2}}}{R_{\mathrm{bi2}}}$ and $F_{\mathrm{bearb2}} = -F_{\mathrm{bearo2}} - F_{\mathrm{beari2}}$. Due to the nonlinear time-varying temperature and thermal resistances, generalized nonlinear bearing thermal forces have complex nonlinear time-varying characteristics with rotation speed, especially at the resonant peaks. Particularly, F_{beari3} decreases from positive values to negative values with the increase in rotation speed. It means that the F_{bearo} and F_{beari} are not always negative according to the temperature relationship among the rolling elements, the inner ring and the outer ring. Unlike radial bearing loads, the shapes of generalized nonlinear bearing thermal force curves

are closer to temperature variations of thermal nodes. They maintain an overall trend of either increase or decrease, rather than sharply increasing only at the resonant peaks.

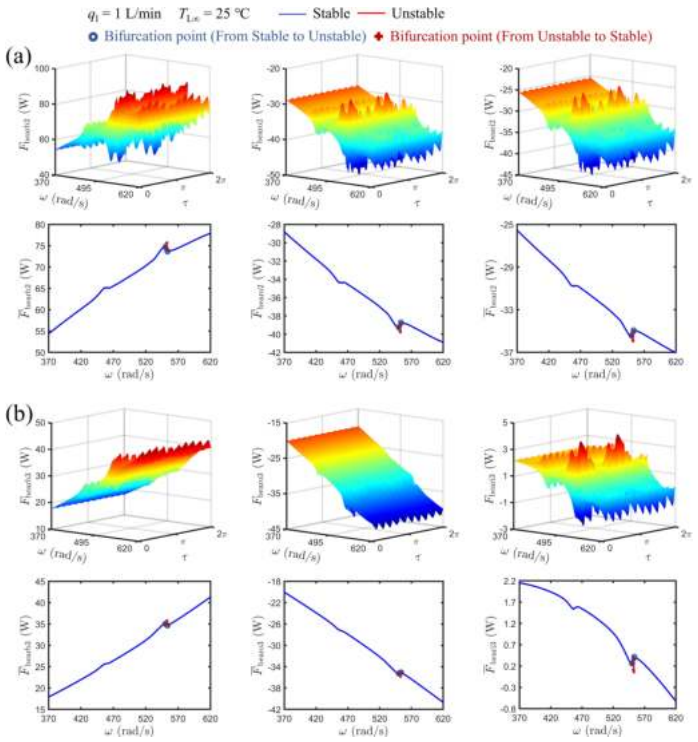

Figure 17: Time-varying and average generalized nonlinear bearing thermal forces (a) of the 2# ball bearing. (b) of the 3# roller bearing. (The blue solid line represents the stable solution, and the red solid line represents the unstable solution).

Fig. 18 shows the time-varying and average viscosities of lubricants with rotation speed for the four bearings. The viscosities decrease with the increase in rotation speed due to the temperature-viscosity relationship of lubricants in Eq. (12). The reason for no significant variations in time-varying viscosities is that there are only small fluctuations in the temperature of lubricants.

Lubricant thermal resistances are calculated based on the lubricant viscosity. Hence, the nonlinear characteristics are significant in average results, but time-varying characteristics are not obvious, as shown in Fig. 19. Similarly taking the 2# ball bearing as an example, there are $F_{\mathrm{lubb2}} = \frac{T_{\mathrm{b2}} - T_{\mathrm{L2}}}{R_{\mathrm{bL2}}}$, $F_{\mathrm{lubo2}} = \frac{T_{\mathrm{o2}} - T_{\mathrm{L2}}}{R_{\mathrm{oL2}}}$, $F_{\mathrm{lubi2}} = \frac{T_{\mathrm{i2}} - T_{\mathrm{L2}}}{R_{\mathrm{iL2}}}$, $F_{\mathrm{lubh2}} = \frac{T_{\mathrm{h2}} - T_{\mathrm{L2}}}{R_{\mathrm{hL2}}}$ and $F_{\mathrm{lubL2}} = -F_{\mathrm{lubb2}} - F_{\mathrm{lubi2}} - F_{\mathrm{lubo2}} - 2F_{\mathrm{lubh2}}$. The 3# roller bearing does not have F_{lubh} according to Fig. 4. It can be found that F_{lubh2} decreases with the increase in rotation speed and is still negative. F_{lubb2} is the absolute dominant component of F_{lubL2}, because it is far

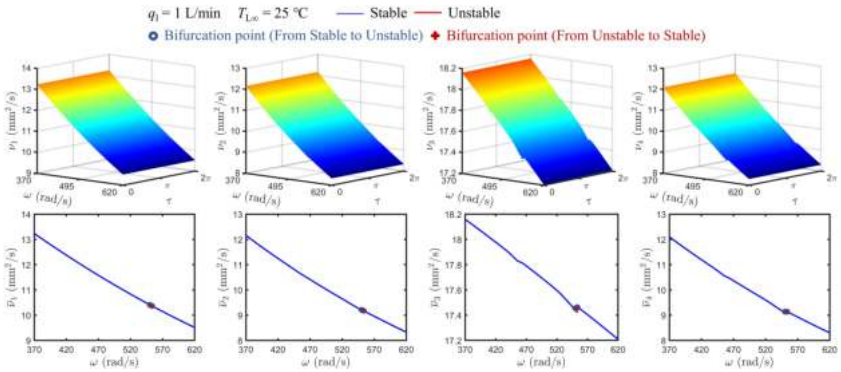

Figure 18: Time-varying and average lubricant viscosities of the four bearings. (The blue solid line represents the stable solution, and the red solid line represents the unstable solution).

larger than F_{lubo2}, F_{lubi2} and F_{lubh2}. On the other hand, the shapes and values of F_{lubo3}, F_{lubi3} and F_{lubi3} are fairly close. The reason for the relationships and variations of these generalized nonlinear lubricant thermal forces can be found in Fig. 14(e).

Time-varying and average generalized nonlinear heat generation/dissipation thermal forces of the 2# ball bearing and the 3# roller bearing are demonstrated in Fig. 20. For the heat generation nonlinear forces, Q_{gl} has similar nonlinear time-varying characteristics as the radial bearing loads in Fig. 16. Q_{gv} has the similar nonlinear characteristics as the lubricant viscosity in Fig. 18. Q_{gv2} dominates the Q_{g2} without obvious time-varying characteristics. Conversely, the difference between Q_{gl3} and Q_{gv3} is not very large, leading to significant nonlinear time-varying characteristics in Q_{g3}. The heat dissipation nonlinear forces Q_{d} are calculated based on the temperature of lubricants. Hence, their nonlinear characteristics are very similar to the lubricant viscosity.

Nonlinearity sources in thermal characteristics are discussed by generalized nonlinear thermal forces in Fig. 16-20. All nonlinearity sources can be divided into two main categories. The first category includes the generalized nonlinear bearing thermal forces and the frictional heat from the load. It is caused by the radial bearing loads with significant nonlinear time-varying characteristics. The second one includes generalized nonlinear lubricant thermal forces and the frictional heat from the lubricant. It is caused by the lubricant viscosity with the significant nonlinear characteristics. Additionally, the generalized nonlinear heat dissipation thermal forces are caused by the temperature of lubricants and have the same nonlinear characteristics as the second category. The various shapes and values of generalized nonlinear thermal forces correspond to the overall temperature variations and temperature sorts of thermal nodes, which can be found in Fig. 14.

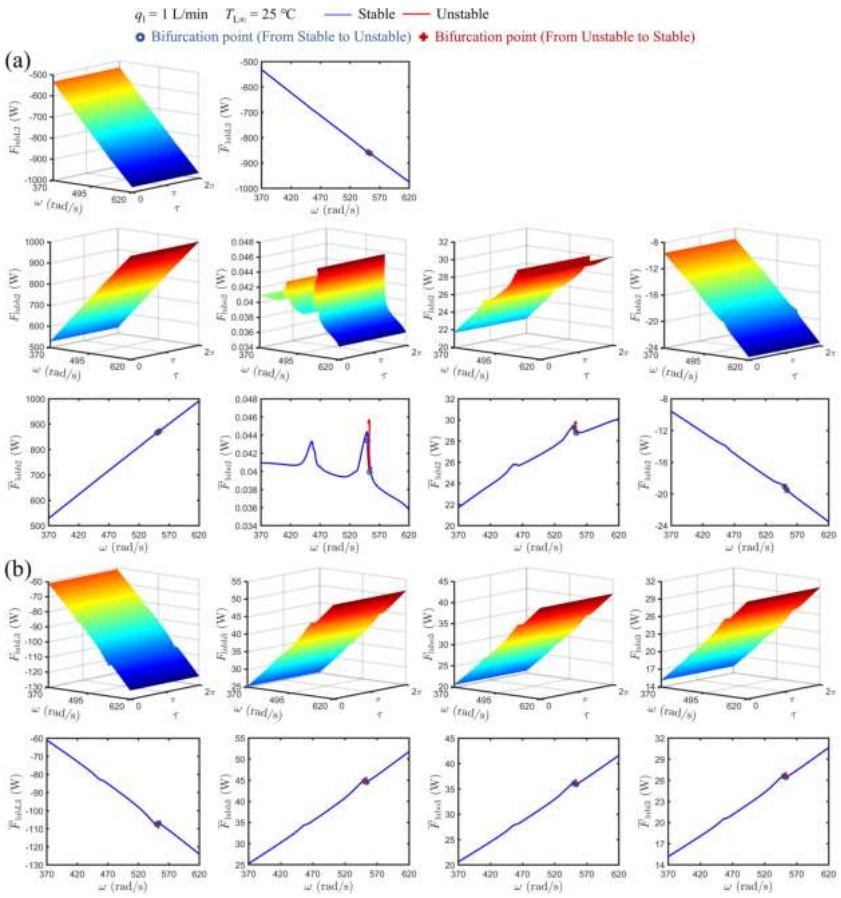

Figure 19: Time-varying and average generalized nonlinear lubricant thermal forces (a) of the 2# ball bearing. (b) of the 3# roller bearing. (The blue solid line represents the stable solution, and the red solid line represents the unstable solution).

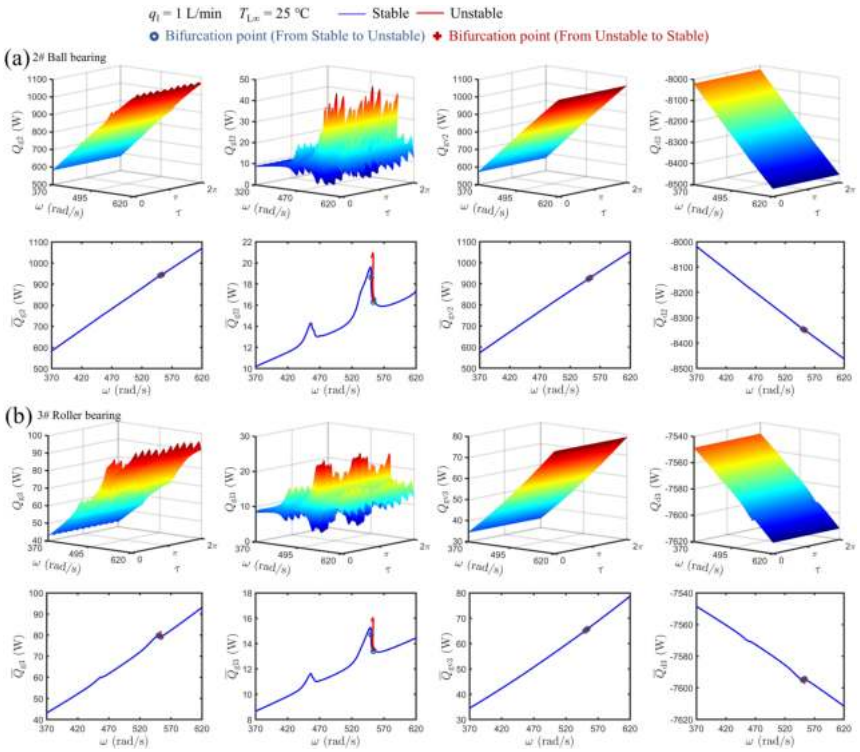

Figure 20: Time-varying and average generalized nonlinear heat generation/dissipation thermal forces with rotation speed (a) of the 2# ball bearing. (b) of the 3# roller bearing. (The blue solid line represents the stable solution, and the red solid line represents the unstable solution).

5.4 Effect of global temperature increase

In addition to the flow rate of lubricants, the lubricant cooling temperature can also affect the temperature of the system. Increasing the lubricant cooling temperature can be considered as global heating of the system. In order to highlight the effect of global temperature increase on the dynamic characteristics of the system more clearly, a slightly simpler case of the high TM coupling degree with $q_l = 2$ L/min is selected as a comparison.

The nonlinear dynamic characteristics with $q_l = 2$ L/min and the lubricant cooling temperature 50 °C is shown in Fig. 21. Comparing Fig. 21 with Fig. 9 and Fig. 11(a), it can be found that the increased lubricant cooling temperature leads to more bifurcation points, more nonlinear phenomena, and larger unstable regions, besides the resonant peaks with lower frequencies and larger vibration responses. There are four saddle-node bifurcation points (see Fig. 21(c)) in the amplitude-frequency responses of the dynamic node 8 and 1. The BP_1 and BP_2 first emerge and create a new resonance hysteresis phenomenon. The BP_3 and BP_4 remain at basically similar rotation speeds as the case of the lubricant cooling temperature 25 °C. Comparing Fig. 21 with the case of the highest TM coupling degree in Fig. 10, there are the same number of bifurcation points. However, no Neimark-Sacker bifurcation points, unstable regions with high vibration response amplitudes, or more complex nonlinear phenomena emerge in the case of global heating, although it has larger effective RCs of the four bearings, due to the effect of rotation speed on temperature being relatively weakened when the system has reached a higher temperature, leading to lower variation velocities and variation ranges of RCs in Fig. 21(b) than that in Fig. 10(b).

Fig. 22 shows the nonlinear thermal characteristics with $q_l = 2$ L/min and the lubricant cooling temperature 50 °C. The lowest temperature is about 50 °C, near the lubricant cooling temperature. The highest temperature is about 72 °C. This means that increasing the lubricant cooling temperature will raise the overall temperature, but the temperature difference with rotation speed is smaller than decreasing the lubricant flow rate in Fig. 14(b). For Fig. 22(b), there are corresponding nonlinear phenomena of temperature variations in the intervals of the bifurcation points. A small looping phenomenon appears at $[\omega_{BP_3}, \omega_{BP_4}]$, which is different from the amplitude-frequency response curve. Compared with the nonlinear temperature variations under different TM coupling degrees, the shapes of temperature variations in Fig. 22(b) are closer to that in Fig. 15(b) rather than in Fig. 15(c). It can be inferred that the lubricant flow rate has a relatively significant effect on temperature variations compared to the lubricant cooling temperature.

6 Conclusions and final remarks

The coupled TM model of a dual-rotor system is proposed, and its nonlinear characteristics after thermal balance are analyzed systematically in this paper.

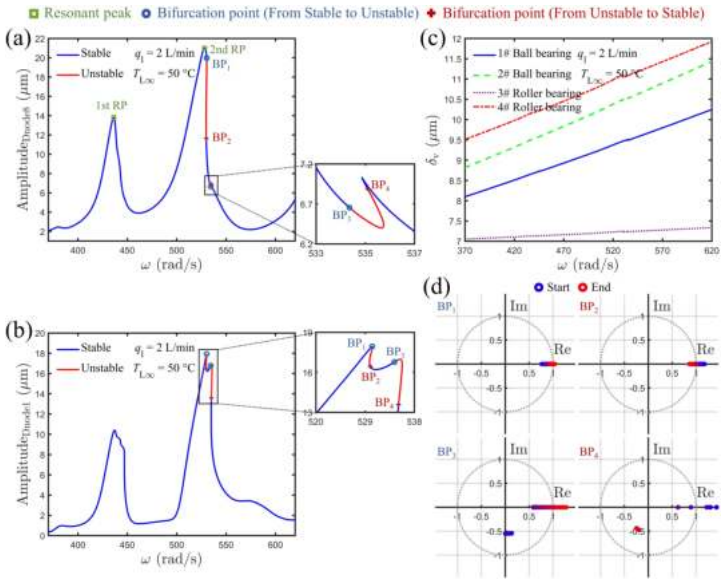

Figure 21: Nonlinear dynamic characteristics with $q_l = 2$ L/min and the lubricant cooling temperature 50 °C. (a-b) Amplitude-frequency responses of the dynamic node 8 and the dynamic node 1, respectively. (The blue solid line represents the stable solution, and the red solid line represents the unstable solution). (c) RC variations of the four bearings. (d) Relationships between the eigenvalues and the unit circle of the bifurcation points.

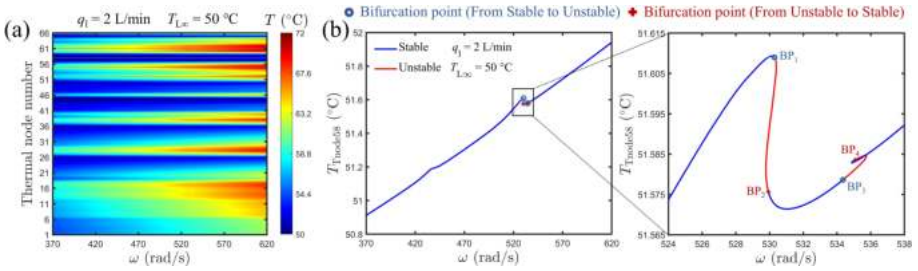

Figure 22: Nonlinear thermal characteristics with $q_l = 2$ L/min and the lubricant cooling temperature 50 °C. (a) Overall temperature variations of thermal nodes with rotation speed. (b) Nonlinear temperature variations of the thermal node 58. (The blue solid line represents the stable solution, and the red solid line represents the unstable solution).

The dynamic model is developed as a discretized one-dimensional continuum using the FE method, and the thermal model is developed using the LPTN method. Multiple nonlinearities and heat generation of four bearings are considered in the model, which couples the mechanical and thermal fields. Coupling degrees are simulated by setting different lubricant flow rates to control the heat dissipation of the system.

The motion and heat balance equations are solved simultaneously by the modified IHB method. Periodic solutions, including unstable ones at primary resonance regions, are obtained. The investigation of nonlinear phenomena and stability evolution of the system is carried out with the increase in TM coupling degrees. Nonlinearity sources in thermal characteristics are discussed by generalized nonlinear thermal forces. The main conclusions are as follows:

(1) Besides shifting the resonance region into a lower frequency direction and inducing larger vibration responses, the resonance regions will emerge with more bifurcation points and larger unstable regions with high vibration response amplitudes as the TM coupling degree increases. Resonance hysteresis phenomena can evolve into more complex nonlinear phenomena. At the same time, stable analysis reveals that some saddle-node bifurcation points can transform into Neimark-Sacker bifurcation points.

(2) The relationship among RC variations under thermal expansion of the four bearings is not fixed with sufficient lubricant flow rates. It will stabilize as $\delta_{v4} > \delta_{v2} > \delta_{v1} > \delta_{v3}$ in a high TM coupling degree, which is consistent with the overall temperature sorts of the system. In the actual operational conditions, the 4# roller bearing needs an independent lubricant inlet channel with the maximum lubricant flow rate, and the 3# inter-shaft roller bearing needs the minimum lubricant flow rate.

(3) The nonlinear thermal characteristics are induced by the radial bearing loads and the lubricant viscosity. Generalized nonlinear bearing thermal forces and the frictional heat from the load are calculated based on the radial bearing loads with significant nonlinear time-varying characteristics. Generalized nonlinear lubricant thermal forces, heat dissipation thermal forces, and the frictional heat from the lubricant are calculated based on the lubricant viscosity or lubricant temperature with significant nonlinear characteristics.

(4) Increasing lubricant cooling temperature can be considered as global heating of the system. It will induce more nonlinear phenomena and more bifurcation points. However, although it has larger effective RCs of bearings compared to the case of the increase in TM coupling degrees, there may be no evolution of bifurcation point types or unstable regions with drastic amplitude changes. This is because the system initially reaches a higher temperature, resulting in smaller variation ranges of RCs with rotation speed.

It is worth mentioning that the IHB method and other harmonic balance methods cannot accurately obtain almost periodic and chaotic solutions. However, they can efficiently determine the bifurcation intervals of the responses combined with the stability discrimination method. Future works will search for evidence of the nonlinear characteristic evolution through experiments.

Acknowledgements

It is very grateful for the National Key R&D Program of China (Grant No. 2023YFE0125900), National Natural Science Foundation of China (Grant No. 12372008), Natural Science Foundation of Heilongjiang Province (Grant No. YQ2022A008), the Fundamental Research Funds for the Central Universities, and the China Scholarship Council (File No. 202306120121).

Data availability

Data will be made available on request.

Declarations

Conflict of interest

The authors declare that they have no conflict of interest.

Appendix

Appendix A

Structure parameters of the 1 # and 2 # ball bearings are given in Table A.1. Structure parameters of the 3 # and 4 # roller bearings are given in Table A.2. Structure parameters of the disks are given in Table A.3. Structure parameters of the shafts are given in Table A.4. The speed ratio of the HP rotor and LP rotor λ is 1.2. The stiffness of the linear elastic support (at dynamic node 4) is 1×10^8 N/m. Material parameters of the rotor are given in Table A.5. Material parameters of the lubricant are given in Table A.6.

Table A.1: Structure parameters of the 1 # and 2 # ball bearings

Physical Parameter	Variable	1 # ball bearing	2 # ball bearing
Inner diameter (m)	d_{b}	140×10^{-3}	134×10^{-3}
Outer diameter (m)	D_{b}	200×10^{-3}	200×10^{-3}
Diameter of inner ring (m)	d_{bi}	150.95×10^{-3}	144.775×10^{-3}
Diameter of outer ring (m)	d_{bo}	189.05×10^{-3}	189.225×10^{-3}
Ball number	N_{ball}	22	20
Pitch diameter (m)	D_{bm}	170×10^{-3}	167×10^{-3}
Width of bearing (m)	B_{b}	24×10^{-3}	22×10^{-3}
Diameter of ball (m)	d_{ball}	19.05×10^{-3}	22.225×10^{-3}
Hertzian contact stiffness ($\mathrm{N/m^{3/2}}$)	k_{b}	1.45×10^{9}	1.57×10^{9}
Initial radial clearance (m)	δ_0	1×10^{-6}	1×10^{-6}
Radius of housing (m)	r_{h}	113.891×10^{-3}	113.891×10^{-3}
Length of housing (m)	l_{h}	160.83×10^{-3}	160.83×10^{-3}
Length of part of housing (m)	l_{hs}	23.755×10^{-3}	23.755×10^{-3}
Inner radius of corresponding shaft element (m)	r_{LP}	53×10^{-3}	54×10^{-3}

Table A.2: Structure parameters of the 3 # and 4 # roller bearings

Physical Parameter	Variable	3 # roller bearing	4 # roller bearing
Inner diameter (m)	d_{r}	120×10^{-3}	130×10^{-3}
Outer diameter (m)	D_{r}	160×10^{-3}	180×10^{-3}
Diameter of inner ring (m)	d_{ri}	128×10^{-3}	143×10^{-3}
Diameter of outer ring (m)	d_{ro}	152×10^{-3}	167×10^{-3}
Roller number	N_{roller}	28	30
Pitch diameter (m)	D_{rm}	140×10^{-3}	155×10^{-3}
Length of roller (m)	a_{roller}	16×10^{-3}	12×10^{-3}
Width of bearing (m)	B_{r}	22×10^{-3}	24×10^{-3}
Diameter of roller (m)	d_{roller}	12×10^{-3}	12×10^{-3}
Hertzian contact stiffness (N/m$^{10/9}$)	k_{r}	1.89×10^{8}	1.46×10^{8}
Initial radial clearance (m)	δ_0	5×10^{-6}	1×10^{-6}
Radius of housing (m)	r_{h}	-	103.188×10^{-3}
Length of housing (m)	l_{h}	-	75.465×10^{-3}
Length of part of housing (m)	l_{hs}	-	10.445×10^{-3}
Inner radius of corresponding shaft element (m)	r_{LP}	56×10^{-3}	50×10^{-3}
Outer radius of corresponding shaft element (m)	r_{HP}	90×10^{-3}	-

Table A.3: Structure parameters of the disks

Physical Parameter	Variable	LPC disk	LPT disk	HPC disk	HPT disk
Mass (kg)	m	101.4624	73.115	94.2194	78.436
Polar moment of inertia (kg·m^2)	J_{p}	6.4725	4.9238	2.900985	3.622343
Diameter moment of inertia (kg·m^2)	J_{d}	3.4921	2.9174	1.901732	1.945878
Eccentricity (m)	e	1×10^{-6}	14×10^{-6}	1×10^{-6}	2×10^{-6}

Table A.4: Structure parameters of the shafts

Shaft element	Inner diameter (m)	Outer diameter (m)	Length (m)
Dynamic node 1 to 2	106×10^{-3}	140×10^{-3}	12×10^{-3}
Dynamic node 2 to 3	112×10^{-3}	120×10^{-3}	198×10^{-3}
Dynamic node 3 to 4	112×10^{-3}	120×10^{-3}	406.8×10^{-3}
Dynamic node 4 to 5	112×10^{-3}	120×10^{-3}	316.5125×10^{-3}
Dynamic node 5 to 6	112×10^{-3}	120×10^{-3}	316.5125×10^{-3}
Dynamic node 6 to 7	112×10^{-3}	120×10^{-3}	316.5125×10^{-3}
Dynamic node 7 to 8	112×10^{-3}	120×10^{-3}	316.5125×10^{-3}
Dynamic node 8 to 9	112×10^{-3}	120×10^{-3}	51×10^{-3}
Dynamic node 9 to 10	112×10^{-3}	120×10^{-3}	27×10^{-3}
Dynamic node 10 to 11	100×10^{-3}	130×10^{-3}	12×10^{-3}
Dynamic node 12 to 13	108×10^{-3}	134×10^{-3}	11×10^{-3}
Dynamic node 13 to 14	130×10^{-3}	164×10^{-3}	444.968×10^{-3}
Dynamic node 14 to 15	130×10^{-3}	164×10^{-3}	299.94×10^{-3}
Dynamic node 15 to 16	130×10^{-3}	164×10^{-3}	299.94×10^{-3}
Dynamic node 16 to 17	130×10^{-3}	164×10^{-3}	123.43×10^{-3}
Dynamic node 17 to 18	160×10^{-3}	180×10^{-3}	11×10^{-3}

Table A.5: Material parameters of the rotor

Physical parameter	Variable	Bearing	Shaft and bearing housing
Elastic modulus (GPa)	E	210	210
Poisson's ratio	μ	0.3	0.3
Density (kg/m^3)	ρ	7.83×10^{3}	7.89×10^{3}
Specific heat capacity (J/(kg·K))	c	450	480
Thermal conductivity (W/(m·K))	k_{D}	45	46.9
Linear expansion coefficient (K^{-1})	Γ	12.03×10^{-6}	12.03×10^{-6}

Table A.6: Material parameters of the lubricant

Physical parameter	Variable	Lubricant
Viscosity-temperature coefficient	β	0.02339
Density (kg/m^3)	ρ_{l}	8.8×10^2
Specific heat capacity (J/(kg·K))	c_{l}	1870
Thermal conductivity (W/(m·K))	k_{l}	0.14
Thermal diffusivity (m^2/s)	α_{l}	7.38×10^{-8}

Appendix B

The mass matrix $\mathbf{M}_{\mathrm{s}}$ is expressed as

$$\begin{aligned}
&\mathbf{M}_{\mathrm{s}} = \mathbf{M}_{\mathrm{sT}} + \mathbf{M}_{\mathrm{sR}},\\
&\mathbf{M}_{\mathrm{sT}} = \frac{\rho A l}{(1+\varphi_{\mathrm{s}})^2}\begin{bmatrix} m_1 & & & \text{sym.}\\ m_2 & m_5 & & \\ m_3 & -m_4 & m_1 & \\ m_4 & m_6 & -m_2 & m_5 \end{bmatrix},\\
&\mathbf{M}_{\mathrm{sR}} = \frac{\rho I}{l(1+\varphi_{\mathrm{s}})^2}\begin{bmatrix} m_7 & & & \text{sym.}\\ m_8 & m_9 & & \\ -m_7 & -m_8 & m_7 & \\ m_8 & m_{10} & -m_8 & m_9 \end{bmatrix},
\end{aligned} \tag{B.1}$$

the inertia matrix $\mathbf{J}_{\mathrm{s}}$ is expressed as

$$\mathbf{J}_{\mathrm{s}} = 2\mathbf{M}_{\mathrm{sR}}, \tag{B.2}$$

and the stiffness matrix $\mathbf{K}_{\mathrm{s}}$ is expressed as

$$\mathbf{K}_{\mathrm{s}} = \frac{EI}{(1+\varphi_{\mathrm{s}})l^3}\begin{bmatrix} 12 & & & \text{sym.}\\ 6l & (4+\varphi_{\mathrm{s}})l^2 & & \\ -12 & -6l & 12 & \\ 6l & (2-\varphi_{\mathrm{s}})l^2 & -6l & (4+\varphi_{\mathrm{s}})l^2 \end{bmatrix}, \tag{B.3}$$

where $\varphi_{\mathrm{s}} = \frac{12EI}{G\kappa A l^2}$, $G = \frac{E}{2(\mu+1)}$, $\kappa = \frac{1}{\frac{7+6\mu}{6(1+\mu)}\left[1+\frac{20+12\mu}{7+6\mu}\left(\frac{Dd}{D^2+d^2}\right)^2\right]}$. $m_1 = \frac{13}{35}+\frac{7}{10}\varphi_{\mathrm{s}}+\frac{1}{3}{\varphi_{\mathrm{s}}}^2$, $m_2 = l(\frac{11}{210}+\frac{11}{120}\varphi_{\mathrm{s}}+\frac{1}{24}{\varphi_{\mathrm{s}}}^2)$, $m_3 = \frac{9}{70}+\frac{3}{10}\varphi_{\mathrm{s}}+\frac{1}{6}{\varphi_{\mathrm{s}}}^2$, $m_4 = -l(\frac{13}{420}+\frac{3}{40}\varphi_{\mathrm{s}}+\frac{1}{24}{\varphi_{\mathrm{s}}}^2)$, $m_5 = l^2(\frac{1}{105}+\frac{1}{60}\varphi_{\mathrm{s}}+\frac{1}{120}{\varphi_{\mathrm{s}}}^2)$, $m_6 = -l^2(\frac{1}{140}+\frac{1}{60}\varphi_{\mathrm{s}}+\frac{1}{120}{\varphi_{\mathrm{s}}}^2)$, $m_7 = \frac{6}{5}$, $m_8 = l(\frac{1}{10}-\frac{1}{2}\varphi_{\mathrm{s}})$, $m_9 = l^2(\frac{2}{15}+\frac{1}{6}\varphi_{\mathrm{s}}+\frac{1}{3}{\varphi_{\mathrm{s}}}^2)$, $m_{10} = l^2(-\frac{1}{30}-\frac{1}{6}\varphi_{\mathrm{s}}+\frac{1}{6}{\varphi_{\mathrm{s}}}^2)$. For each shaft element, ρ is the density, A is the area of the cross-section, l is the length, E is the elastic modulus, I is the moment of inertia, μ is the Poisson's ratio, D is the outer diameter, d is the inner diameter.

Appendix C

The generalized thermal damping matrix is expressed as

$$\mathbf{C}_{\mathrm{T}} = \begin{bmatrix} m_1c_1 & 0 & \cdots & 0 & \cdots & 0 \\ 0 & m_2c_2 & \cdots & 0 & \cdots & 0 \\ \vdots & \vdots & \ddots & \vdots & \ddots & \vdots \\ 0 & 0 & \cdots & m_pc_p & \cdots & 0 \\ \vdots & \vdots & \ddots & \vdots & \ddots & \vdots \\ 0 & 0 & \cdots & 0 & \cdots & m_nc_n \end{bmatrix}. \tag{C.1}$$

The generalized thermal stiffness matrix is expressed as

$$\mathbf{K}_{\mathrm{T}} = \begin{bmatrix} \sum_{j}^{N_j} \frac{1}{R_{1-j}} & -\frac{1}{R_{1-2}} & \cdots & -\frac{1}{R_{1-p}} & \cdots & -\frac{1}{R_{1-n}} \\ -\frac{1}{R_{2-1}} & \sum_{j}^{N_j} \frac{1}{R_{2-j}} & \cdots & -\frac{1}{R_{2-p}} & \cdots & -\frac{1}{R_{2-n}} \\ \vdots & \vdots & \ddots & \vdots & \ddots & \vdots \\ -\frac{1}{R_{p-1}} & -\frac{1}{R_{p-2}} & \cdots & \sum_{j}^{N_j} \frac{1}{R_{p-j}} & \cdots & -\frac{1}{R_{p-n}} \\ \vdots & \vdots & \ddots & \vdots & \ddots & \vdots \\ -\frac{1}{R_{n-1}} & -\frac{1}{R_{n-2}} & \cdots & -\frac{1}{R_{n-p}} & \cdots & \sum_{j}^{N_j} \frac{1}{R_{n-j}} \end{bmatrix}. \tag{C.2}$$

References

[1] Fu C, Zhang K, Cheng H, Zhu W, Zheng Z, Lu K, Yang Y (2024) A comprehensive study on natural characteristics and dynamic responses of a dual-rotor system with inter-shaft bearing under non-random uncertainty. Journal of Sound and Vibration 570:118091, DOI 10.1016/j.jsv.2023.118091

[2] Xu H, Yang Y, Ma H, Luo Z, Li X, Han Q, Wen B (2022) Vibration characteristics of bearing-rotor systems with inner ring dynamic misalignment. International Journal of Mechanical Sciences 230:107536, DOI 10.1016/j.ijmecsci.2022.107536

[3] Chen Y, Hou L, Chen G, Song H, Lin R, Jin Y, Chen Y (2023) Nonlinear dynamics analysis of a dual-rotor-bearing-casing system based on a modified HB-AFT method. Mechanical Systems and Signal Processing 185:109805, DOI 10.1016/j.ymssp.2022.109805

[4] Jin Y, Zhou X, Quan X, Zhang X, Lu K, Wang J (2024) Topological structures of vibration responses for dual-rotor aeroengine. Mechanical Systems and Signal Processing 208:111053, DOI 10.1016/j.ymssp.2023.111053

[5] Hou L, Chen Y, Fu Y, Chen H, Lu Z, Liu Z (2017) Application of the HB-AFT method to the primary resonance analysis of a dual-rotor system. Nonlinear Dynamics 88(4):2531–2551, DOI 10/gbhtg7

[6] Chen Y, Hou L, Lin R, Wang Y, Saeed NA, Chen Y (2024) Combination resonances of a dual-rotor-bearing-casing system. Nonlinear Dynamics DOI 10.1007/s11071-024-09282-8

[7] Hou L, Chen Y, Chen Y (2023) Combination resonances of a dual-rotor system with inter-shaft bearing. Nonlinear Dynamics 111(6):5197–5219, DOI 10.1007/s11071-022-08133-8

[8] Li Q, Chen C, Gao S, Ren Y, Wang W (2022) The coupled bending-torsional dynamic behavior in the rotating machinery: Modeling, simulation and experiment validation. Mechanical Systems and Signal Processing 178:109306, DOI 10.1016/j.ymssp.2022.109306

[9] Chang Z, Hou L, Lin R, Jin Y, Chen Y (2023) A modified IHB method for nonlinear dynamic and thermal coupling analysis of rotor-bearing systems. Mechanical Systems and Signal Processing 200:110586, DOI 10.1016/j.ymssp.2023.110586

[10] Cai J, Xiang G, Li S, Guo J, Wang J, Chen S, Yang T (2022) Mathematical modeling for nonlinear dynamic mixed friction behaviors of novel coupled bearing lubricated with low-viscosity fluid. Physics of Fluids 34(9):093612, DOI 10.1063/5.0108943

[11] Silvestri P, Reggio F, Niccolini Marmont Du Haut Champ CA, Ferrari ML, Massardo AF (2022) Compressor Surge Precursors for a Turbocharger Coupled to a Pressure Vessel. Journal of Engineering for Gas Turbines and Power DOI 10.1115/1.4055479

[12] Tan X, He J, Xi C, Deng X, Xi X, Chen W, He H (2021) Dynamic modeling for rotor-bearing system with electromechanically coupled boundary conditions. Applied Mathematical Modelling 91:280–296, DOI 10.1016/j.apm.2020.09.042

[13] Gupta PK (2011) Current status of and future innovations in rolling bearing modeling. Tribology Transactions 54(3):394–403, DOI 10.1080/10402004.2010.551805

[14] Cao H, Niu L, Xi S, Chen X (2018) Mechanical model development of rolling bearing-rotor systems: A review. Mechanical Systems and Signal Processing 102:37–58, DOI 10.1016/j.ymssp.2017.09.023

[15] Takabi J, Khonsari MM (2015) On the thermally-induced seizure in bearings: A review. Tribology International 91:118–130, DOI 10/f7skq3

[16] Bossmanns B, Tu JF (1999) A thermal model for high speed motorized spindles. International Journal of Machine Tools and Manufacture 39(9):1345–1366, DOI 10.1016/S0890-6955(99)00005-X

[17] Kim SM, Lee KJ, Lee SK (2002) Effect of bearing support structure on the high-speed spindle bearing compliance. International Journal of Machine Tools and Manufacture 42(3):365–373, DOI 10.1016/S0890-6955(01)00126-2

[18] Takabi J, Khonsari MM (2013) Experimental testing and thermal analysis of ball bearings. Tribology International 60:93–103, DOI 10.1016/j.triboint.2012.10.009

[19] Hao X, Zhai J, Liang J, Chen Y, Han Q (2020) Time-varying stiffness characteristics of roller bearing influenced by thermal behavior due to surface frictions and different lubricant oil temperatures. Tribology International 144:106125, DOI 10.1016/j.triboint.2019.106125

[20] Jin C, Zhu Y, Xu L, Xu Y, Zheng Y (2015) The thermodynamic properties of a new type catcher bearing used in active magnetic bearings system. Applied Thermal Engineering 82:253–263, DOI 10.1016/j.applthermaleng.2015.02.076

[21] Mahner M, Bauer M, Schweizer B (2021) Numerical analyzes and experimental investigations on the fully-coupled thermo-elasto-gasdynamic behavior of air foil journal bearings. Mechanical Systems and Signal Processing 149:107221, DOI 10.1016/j.ymssp.2020.107221

[22] Yan K, Hong J, Zhang J, Mi W, Wu W (2016) Thermal-deformation coupling in thermal network for transient analysis of spindle-bearing system. International Journal of Thermal Sciences 104:1–12, DOI 10.1016/j.ijthermalsci.2015.12.007

[23] Xie Z, Zhu W (2022) An investigation on the lubrication characteristics of floating ring bearing with consideration of multi-coupling factors. Mechanical Systems and Signal Processing 162:108086, DOI 10.1016/j.ymssp.2021.108086

[24] Wang K, Wang C, Wang X, Zhu K, Yang L (2024) Nonlinear tribodynamic performance and transient stability for marine dynamically loaded offset-halves journal bearings. Tribology International 191:109177, DOI 10.1016/j.triboint.2023.109177

[25] Gao S, Chatterton S, Pennacchi P, Han Q, Chu F (2022) Skidding and cage whirling of angular contact ball bearings: Kinematic-hertzian contact-thermal-elasto-hydrodynamic model with thermal expansion and experimental validation. Mechanical Systems and Signal Processing 166:108427, DOI 10.1016/j.ymssp.2021.108427

[26] Xiang G, Wang J, Han Y, Yang T, Dai H, Yao B, Zhou C, Wang L (2022) Investigation on the nonlinear dynamic behaviors of water-lubricated bearings considering mixed thermoelastohydrodynamic performances. Mechanical Systems and Signal Processing 169:108627, DOI 10.1016/j.ymssp.2021.108627

[27] Liu Y, Chen Z, Zhai W, Lei Y (2024) Investigation on skidding behavior of a lubricated rolling bearing with fluid–solid-heat coupling effect. Mechanical Systems and Signal Processing 206:110922, DOI 10.1016/j.ymssp.2023.110922

[28] Goldman P, Muszynska A (1995) Rotor-to-stator, rub-related, thermal-mechanical effects in rotating machinery. Chaos Solitons & Fractals 5(9):1579–1601, DOI 10.1016/0960-0779(94)00165-M

[29] Kumar R, Kumar VS, Butt MM, Sheikh NA, Khan SA, Afzal A (2020) Thermo-mechanical analysis and estimation of turbine blade tip clearance of a small gas turbine engine under transient operating conditions. Applied Thermal Engineering 179:115700, DOI 10.1016/j.applthermaleng.2020.115700

[30] Liu H, Zhang Y, Li C, Li Z (2021) Nonlinear dynamic analysis of CNC lathe spindle-bearing system considering thermal effect. Nonlinear Dynamics 105(1):131–166, DOI 10.1007/s11071-021-06613-x

[31] Sun Z, Chen S, Hu Z, Lei D (2022) Vibration response analysis of a gear-rotor-bearing system considering steady-state temperature. Nonlinear Dynamics 107(1):477–493, DOI 10.1007/s11071-021-07024-8

[32] Chang-Jian CW (2023) Bifurcation analysis of a rotor-bearing system with temperature-dependent viscosity. Journal of Low Frequency Noise, Vibration and Active Control p 14613484231206336, DOI 10.1177/14613484231206336

[33] Wang R, Wang Q, Guan X, Shao W (2022) The coupling free vibration characteristics of a rotating functionally graded shaft-disk system in thermal field. Thin-Walled Structures 176:109278, DOI 10.1016/j.tws.2022.109278

[34] Gao P, Chen Y, Hou L (2020) Nonlinear thermal behaviors of the inter-shaft bearing in a dual-rotor system subjected to the dynamic load. Nonlinear Dynamics 101(1):191–209, DOI 10/gmvk8r

[35] Nicholas TEW, Scobie JA, Lock GD, Tang H (2023) A model of mass and heat transfer for disc temperature prediction in open compressor cavities. Journal of Turbomachinery 146(041001), DOI 10.1115/1.4064082

[36] Nicholas TEW, Pernak MJ, Scobie JA, Lock GD, Tang H (2023) Transient heat transfer and temperatures in closed compressor rotors. Applied Thermal Engineering 230:120759, DOI 10.1016/j.applthermaleng.2023.120759

[37] Sun G, Palazzolo A, Provenza A, Lawrence C, Carney K (2008) Long duration blade loss simulations including thermal growths for dual-rotor gas turbine engine. Journal of Sound and Vibration 316(1-5):147–163, DOI 10/fg4c7z

[38] Neisi N, Heikkinen JE, Sopanen J (2019) Influence of surface waviness in the heat generation and thermal expansion of the touchdown bearing. European Journal of Mechanics - A/Solids 74:34–47, DOI 10.1016/j.euromechsol.2018.10.014

[39] Liu J, Li F, Yong J, Lai T, Zhang P (2020) Investigation of spindle-tool assembly dynamics for optical grinding motorized spindles. Optik 216:164836, DOI 10.1016/j.ijleo.2020.164836

[40] Hu B, Zhou C, Wang H, Chen S (2021) Nonlinear tribo-dynamic model and experimental verification of a spur gear drive under loss-of-lubrication condition. Mechanical Systems and Signal Processing 153:107509, DOI 10.1016/j.ymssp.2020.107509

[41] Peixoto TF, Nordmann R, Cavalca KL (2021) Dynamic analysis of turbochargers with thermo-hydrodynamic lubrication bearings: Abstract. Journal of Sound and Vibration 505:116140, DOI 10.1016/j.jsv.2021.116140

[42] Liu Y, Wang B, Yang S, Liao Y, Guo T (2022) Characteristic analysis of mechanical thermal coupling model for bearing rotor system of high-speed train. Applied Mathematics and Mechanics-English Edition 43(9):1381–1398, DOI 10.1007/s10483-022-2893-5

[43] Gao P, Zhang Z, Dai Q, Jin Y, Hou L, Chen Y (2023) Nonlinear thermo-mechanic coupling effect of a dual-rotor system with an intershaft bearing. Nonlinear Dynamics 111:15933—-15953, DOI 10.1007/s11071-023-08709-y

[44] Gong X, Li C, Xu M, Song W, Liu M, Hao J (2023) Temperature field modeling and vibratory-thermal coupling analysis of ball screw feed system. Thermal Science and Engineering Progress 45:102105, DOI 10.1016/j.tsep.2023.102105

[45] Hao J, Li C, Song W, Yao Z, Miao H, Xu M, Gong X, Lu H, Liu Z (2023) Thermal-mechanical dynamic interaction in high-speed motorized spindle considering nonlinear vibration. International Journal of Mechanical Sciences 240:107959, DOI 10.1016/j.ijmecsci.2022.107959

[46] Hassini MA (2023) Numerical and experimental analysis of stable, unstable, and limit cycle spiral vibrations. Mechanical Systems and Signal Processing 193:110258, DOI 10.1016/j.ymssp.2023.110258

[47] Chang Z, Hou L, Chen Y (2023) Nonlinear dynamics and thermal bidirectional coupling characteristics of a rotor-ball bearing system. Applied Mathematical Modelling 119:513–533, DOI 10.1016/j.apm.2023.03.009

[48] Manoach E, Warminski J, Kloda L, Warminska A, Doneva S (2022) Nonlinear vibrations of a bi-material beam under thermal and mechanical loadings. Mechanical Systems and Signal Processing 177:109127, DOI 10.1016/j.ymssp.2022.109127

[49] Timoshenko SP, Goodier JN (1987) Theory of Elasticity, third ed. edn. McGraw-Hill, New York

[50] Harris TA, Kotzalas MN (2006) Rolling Bearing Analysis: Essential Concepts of Bearing Technology, fifth ed. edn. CRC press, Boca Raton

[51] Jang JY, Khonsari MM, Pascovici MD (1998) Modeling aspects of a rate-controlled seizure in an unloaded journal bearing. Tribology Transactions 41:481–488, DOI 10.1080/10402009808983772

[52] Nakajima K (1995) Thermal contact resistance between balls and rings of a bearing under axial, radial, and combined loads. Journal of Thermophysics and Heat Transfer 9:88–95, DOI 10.2514/3.632

[53] Fand RM (1965) Heat transfer by forced convection from a cylinder to water in crossflow. International Journal of Heat & Mass Transfer 8(7):995–1010, DOI 10.1016/0017-9310(65)90084-0

[54] Bjorklund IS, Kays WM (1959) Heat transfer between concentric rotating cylinders. Journal of Heat Transfer 81:175–186, DOI 10.1115/1.4008173

[55] Cobb EC, Saunders OA (1956) Heat transfer from a rotating disk. Proceedings of the Royal Society of London 236:343–351, DOI 10.1098/rspa.1956.0141

[56] Ricci R, Pennacchi P (2012) Discussion of the dynamic stability of a multi-degree-of-freedom rotor system affected by a transverse crack. Mechanism and Machine Theory 58:82–100, DOI 10.1016/j.mechmachtheory.2012.08.002

[57] Guo C, AL-Shudeifat MA, Yan J, Bergman LA, McFarland DM, Butcher EA (2013) Stability analysis for transverse breathing cracks in rotor systems. European Journal of Mechanics - A/Solids 42:27–34, DOI 10.1016/j.euromechsol.2013.04.001